Optical Coherence Tomography Image Analysis of Corneal Tissue

by

Shiva Zaboli

A thesis
presented to the University of Waterloo
in fulfillment of the
thesis requirement for the degree of
Master of Applied Science
in
Systems Design Engineering

Waterloo, Ontario, Canada, 2011

I hereby declare that I am the sole author of this thesis. This is a true copy of the thesis, including any required final revisions, as accepted by my examiners.

I understand that my thesis may be made electronically available to the public.

Abstract

Because of the ubiquitous use of contact lenses, there is considerable interest in better understanding the anatomy of the cornea, the part of the eye in contact with an exterior lens. The recent technology developments in high resolution Optical Coherence Tomography (OCT) devices allows for the in-vivo observation of the structure of the human cornea in 3D and at cellular level resolution.

Prolonged wear of contact lenses, inflammations, scarring and diseases can change the structure and physiology of the human cornea. OCT is capable of in-vivo, non-contact, 3D imaging of the human cornea. In this research, novel image processing algorithms were developed to process OCT images of the human cornea, in order to determine the corneal optical scattering and transmission. The algorithms were applied to OCT data sets acquired from multiple subjects before, during and after prolonged (3 hours) wear of soft contact lenses and eye patches, in order to investigate the changes in the corneal scattering associated with hypoxia. Results from this study demonstrate the ability of OCT to measure the optical scattering of corneal tissue and to monitor its changes resulting from external stress (hypoxia).

Acknowledgements

I would like to thank my supervisors, Dr. Paul Fieguth and Dr. Kastadinka Bizheva, for their great guidance, assistance and support in my research. I would like to thank my husband, Arash Tabibiazar, for his sacrifices, endless support and encouragement during my studies. This thesis would not have done without him. I would also like to thank my parents, who always had confidence in me and bring me up to this point of life. And last but by no means least, I would like to thank to my patient and understanding daughter, Parmis, who is the most important person in my life.

Dedication

This work is dedicated to my family and, especially, to my husband, Arash Tabibiazar. Without your support and encouragement, this work would not have been possible.

Table of Contents

List of Figures

Chapter 1

Introduction

Optical coherence tomography (OCT) technology [15] is widely used to acquire the inner structure of biological tissue such as the human cornea. Prolonged contact lens wear causes hypoxia in the human cornea that results in changes of overall thickness and transparency of the cornea. Hypoxia induced corneal thickness changes have been observed and quantified with an ultrahigh resolution optical coherence tomography (UHR-OCT) system and an automatic segmentation algorithm [17, 21].

For normal vision, it is imperative that the cornea maintains its high degree of transparency and its physical characteristics, so the precise measurement of the thickness and transparency of all cornea layers is essential for the analysis of corneal swelling, acidosis, and altered corneal oxygen consumption. As the cornea obtains oxygen directly from the air, and the contact lens lies between the cornea and the outside air, an in-vivo study of the cornea and its response to contact lens is of considerable interest.

Contact lens induced hypoxia, inflammation, injuries and degenerative pathologies may alter the optical clarity of the human cornea, reducing its transmission and resulting in blurred vision. Corneal clarity can be quantified by metrics such as optical scattering, absorption, or total attenuation (the sum of absorption and scattering). A number of studies have been conducted in the past for measuring the optical scatter or total attenuation coefficient of normal, healthy corneas by the use of low resolution OCT systems [15, 20]. Several factors may affect the precision of the extracted total attenuation coefficient, which were not accounted in those studies [63]:

- limited axial OCT resolution, which would not allow to resolve the thin corneal layers, such as Bowman's and Descemet's membranes and would lead to imprecise corneal or stromal thickness measurements;

- spatial variations of the image contrast in corneal tomograms related to the natural curvature of the cornea and focusing of the imaging beam.

The object of this thesis is to develop image processing algorithms that would allow for precise measurement of the optical properties, specifically scattering and total attenuation of the human corneal stroma in healthy human cornea under normal condition and hypoxic stress.

An automatic corneal segmentation has been developed and implemented to straighten the corneal image and extract the stromal. A semi automatic segmentation algorithm [25, 34] has been used in the previous works [17, 7] to segment the cornea but in this thesis, a corneal straightening is achieved by segmenting the high-contrast epithelium layer and then straightening the epithelium layer. The epithelium layer has been detected by using an automatic edge detection algorithm [22, 68], then by using the epithelium layer's curve the corneal image will be flattened.

We have developed a novel method that may improve the quality of corneal OCT tomograms by accounting for the natural curvature of the cornea and by focusing on the imaging beam, when applied to UHR-OCT corneal images (OCT axial resolution $< 5\mu m$), it enhances the image contrast to measure the stromal thickness with high precision, and calculates the total stromal attenuation coefficient using Beer-Lambert's law.

In this thesis, we have used hypoxia data to be able to test how our algorithms perform under different conditions and can they provide statistically significant measure of the attenuation changes caused by the hypoxia. We have used a database of OCT corneal images for eight individuals by placing a soft contact lens over the eye to induce corneal edema, then the eye patched for three hours. Following the removal of the lens, a set of ten images is acquire every 15 minutes over a period of two hours. Due to variations between individuals, over time, and instrument settings, significant variations exist in the intensity pattern of the optical beam. A statistical analysis on the stromal intensity, fitting a distribution to the observed spatial variations, led to final assessments of attenuation variation.

Some basic concepts about optics and image processing are explained in Chapters 2 and 3, respectively. The problem formulation is described in Chapter 4, Chapter 5 demonstrates the proposed method. The experimental results are classified to statistical and hypoxia results and explained in Chapters 6 and finally the conclusions and future work are discussed in Chapter 7.

Chapter 2

Background – Optics

Contact lens induced hypoxia, inflammation, injuries and degenerative pathologies can alter the optical clarity of the human cornea, reducing its transmission and resulting in blurred vision. Corneal clarity can be quantified by the use of metrics such as optical scatter, absorption, or total attenuation which all are parts of the propagation properties of light. A number of studies [15, 20, 63] have been conducted in the past for measuring the optical scatter or total attenuation coefficient of normal, healthy corneas by the use of low resolution OCT systems. In this chapter we review the basic concepts of optics in physics which are related to our study. Since we work on corneal optical coherence tomography (OCT), we need to be familiar with this technique. First, we briefly explain corneal anatomy then describe ultrahigh resolution optical coherence tomography technique which is used in corneal imaging. Finally, we explain the propagation properties of light.

2.1 Corneal Anatomy

The quantitative characterization of corneal structure can play an important role in clinical studies and opthalmologic research for studying a variety of corneal pathologies. The cornea is a transparent, avascular front part of the eye wall having a thickness of approximately 0.5 mm in humans which provides almost seventy percent of the refractive power in the eye. It protects the rest of the eye from germs and harmful matter [7] and acts as the outermost layer of the eye (Figure 2.1(a)).

The human cornea consists of five layers, which are shown in Figure 2.1(b); the epithelium is the cornea's outermost region, comprising about ten percent of its thickness. Bowman's layer, stroma, Descement's membrane and endothelium are other layers of cornea.

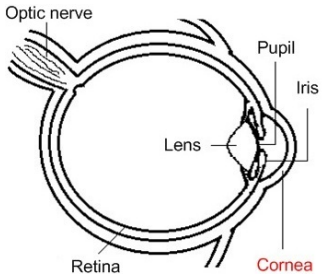

(a) Anatomy of eye

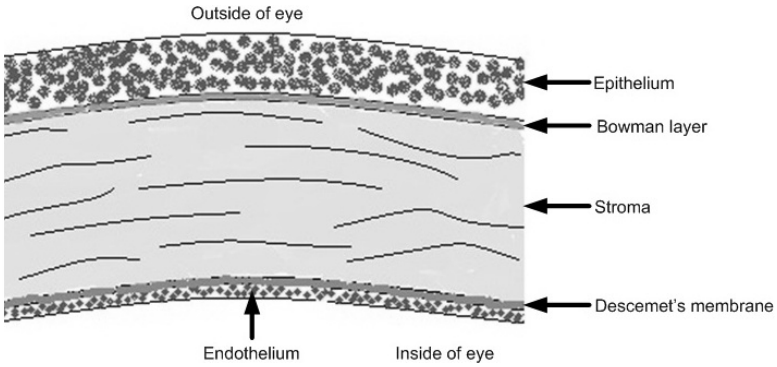

(b) Human corneal layers

Figure 2.1: The cornea is located at the outermost layer of eye (2.1(a)); The human cornea consists of five obvious layers. For questions of corneal swelling, the most relevant part of the structure is the stroma (2.1(b)).

In this thesis our main focus will be on the stromal layer. Approximately ninety percent of the corneal thickness comprises of a region known as the stroma, a layered structure that is made up of many stacked sheets known as lamellae, with corneal cells interspersed between the lamellae making up about three to five percent of the total volume of the stroma. The stroma consists of seventy eight percent of water, and sixteen percent of collagen. When corneal hypoxia is induced by wear of contact lens, it is observed that the corneal thickness increases since the amount of water in the stroma is raised. This alteration affects corneal transparency and corneal physical characteristics, such as thickness.

In order to preserve normal vision, it is imperative that the cornea maintains its high degree of transparency and its physical characteristics so the precise measurement of the thickness and transparency of all cornea layers is essential for the analysis of corneal swelling, acidosis which is increased acidity in tissue, and altered corneal oxygen consumption. Because the cornea obtains oxygen directly from the air, and because contact

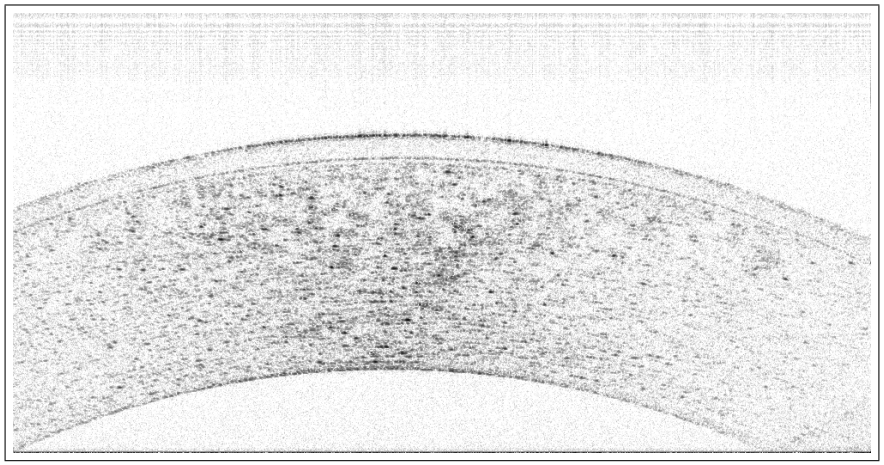

Figure 2.2: Sample image of a human cornea measured in-vivo with ultrahigh resolution optical coherence tomography, with the image showing many of the structural elements sketched in Figure 2.1(b).

lenses lie between the cornea and the outside air, an in-vivo study of the cornea and its response to contact lenses is of considerable interest.

Clinically, we can use the existing optical coherence tomography (OCT) technology [7, 14, 15, 20, 21, 47] to extract the corneal inner structure. Because of the cornea consists mainly water, optical images of the cornea have low signal to noise ratio. Figure 2.2 shows an example of the human cornea acquired with ultra high resolution OCT.

2.2 Optical Coherence Tomography (OCT)

Optical coherence tomography is a noninvasive cross-sectional, high resolution imaging technique [15] for imaging the structure of biological tissues. The principle of operation of OCT is based on low coherence interferometry. Similarly to ultrasound, OCT is able to create a two dimensional image of the internal micro-structure of tissue, analogous to by measuring the amount of reflected light and its location within the imaged tissue sample [20].

A high speed, compact, fiber-optic spectral domain OCT (SD-OCT) system was designed and built in Dr. Bizheva's research lab at the University of Waterloo for human ocular imaging in the 1060nm wavelength range [7, 21, 47]. A schematic of the imaging system is presented in Figure 2.3. The core of the system (a fiber-based Michelson inter-

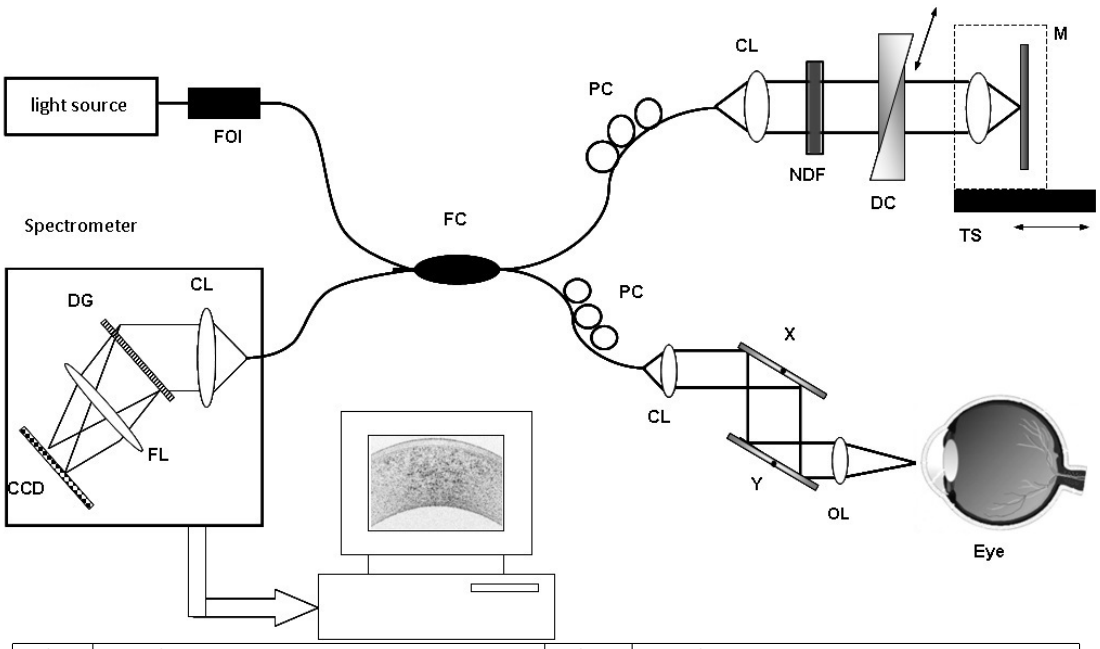

abv	explanation	abv	explanation
CL	collimator lens	DC	dispersion compensation
DG	diffraction grating	FL	focusing lens
OL	ocular lens	PC	polarization controllers
TS	computerized translation stage	X,Y	galvanometric scanning mirror

Figure 2.3: A schematic diagram of the UHR-OCT system [21]. Such an imaging device has been designed and built at the University of Waterloo, and was used to collect the data of Figure 2.2.

ferometer) was interfaced to a broad bandwidth super luminescent diode (SLD, Superlum, λ_c=1022 nm, $\Delta\lambda$=109 nm and P_{out}=9 mW). All optical and fiber optic components were selected to allow for the broad spectrum propagation through the entire SD-OCT system with minimal spectral and power losses. The interference signal was detected by a high efficiency spectrometer (P&P Optica Inc.) and a 1024 pixel linear array CCD camera (Sensors Unlimited-Goodrich) with a 47 kHz readout rate.

An optical imaging probe (Figure 2.4), comprised of a collimator, a pair of galvanometric scanners and a pair of achromat lenses, was designed and built [21] specifically for high resolution imaging of the cornea. The imaging interface was integrated into a modified slit lamp with a chin rest support to allow for easy alignment of the imaging beam and minimization of motion artifacts associated with head movement. A visual target comprised of

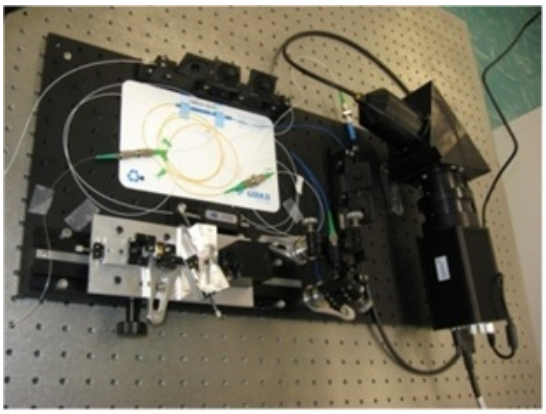

(a) The core of the UHR SD-OCT system [21]

(b) the modified slit lamp biomicroscope with the ocular surface imaging interface [21]

Figure 2.4: Two main parts of the UHR SD-OCT system [21]which is designed and built at the University of Waterloo for human ocular imaging in the 1060nm wavelength range.

9 red LEDs was used to allow subjects to fixate in a forward direction aligned with the axis of the imaging beam or at chosen angles with respect to it. The 2D UHR-OCT tomograms were processed in MATLAB. This UHR-OCT system was used to image non-invasively human corneas in healthy voluntears under natural conditions and hypoxic stress induced by three hours long wear of a soft contact lens and an eye patch to limit oxygen delivery to the cornea.

By measuring the interference between the backscattered light from the sample and the light from the reference mirror, the distance and magnitude of optical scattering within the sample can be measured within micrometers. Scanning the light beam across the sample and recording the magnitude of the interference produces a complete cross-sectional image. OCT images are subject to substantial speckle noise [48], which is a random pattern that affects image intensity. Our goal is to use methods of statistical image processing [16, 18, 65] to extract a measure of the optical attenuation (scattering + absorption) from the corneal OCT images.

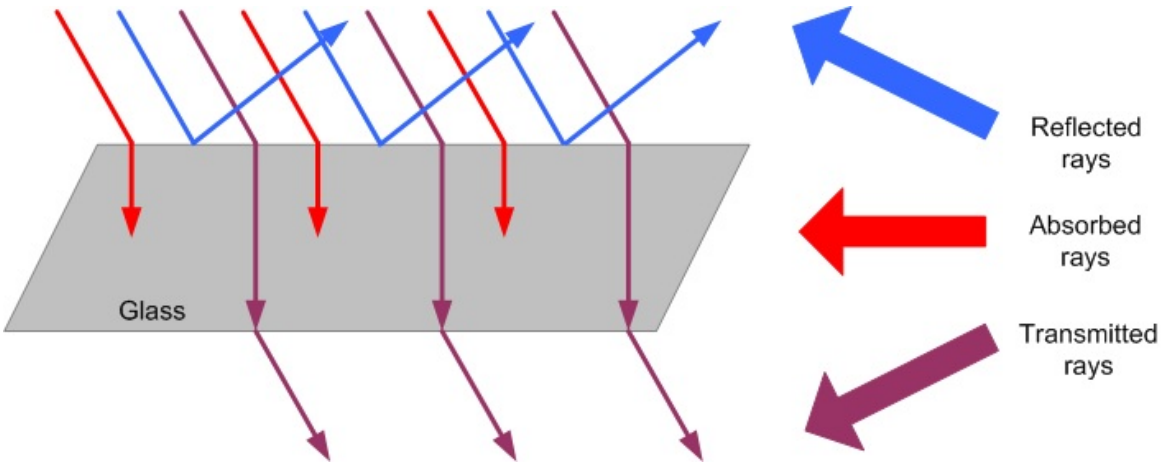

Figure 2.5: When light passes through a material, such as the cornea, it can be scattered, absorbed or transmitted.

2.3 Propagation Properties of Light

Light scattering, absorption and attenuation are part of propagation properties of light which are used to measure corneal clarity. A beam of light on a material can be scattered [24], absorbed or transmitted. Light is transmitted when it emerges, in the same direction as the incident light. Similarly light is scattered when it comes out in a different direction from the incident light. Also light is absorbed when it comes in and its enegy is captured by matter. Scattering and absorption take place at the molecular and atomic level. Figure 2.5 shows these concepts.

2.3.1 Beer-Lambert law

The stromal attenuation coefficient is calculated using Beer-Lambert's law [53, 56]. In optics, the Beer-Lambert law relates the attenuation of light to the physical properties of the material through which light is traveling. The law shows an exponential dependence between the transmission of light, the attenuation coefficient, that acounts both for scattering and absorption of light, the coefficient of the substance and the distance the light travels through the material:

$$I(\lambda) = I_0(\lambda)e^{-\mu(\lambda)d} \tag{2.1}$$

where μ is linear attenuation coefficient and a function of the wavelength λ, I_0 and I are the intensity of the incident and transmitted light, respectively, and d is the physical distance

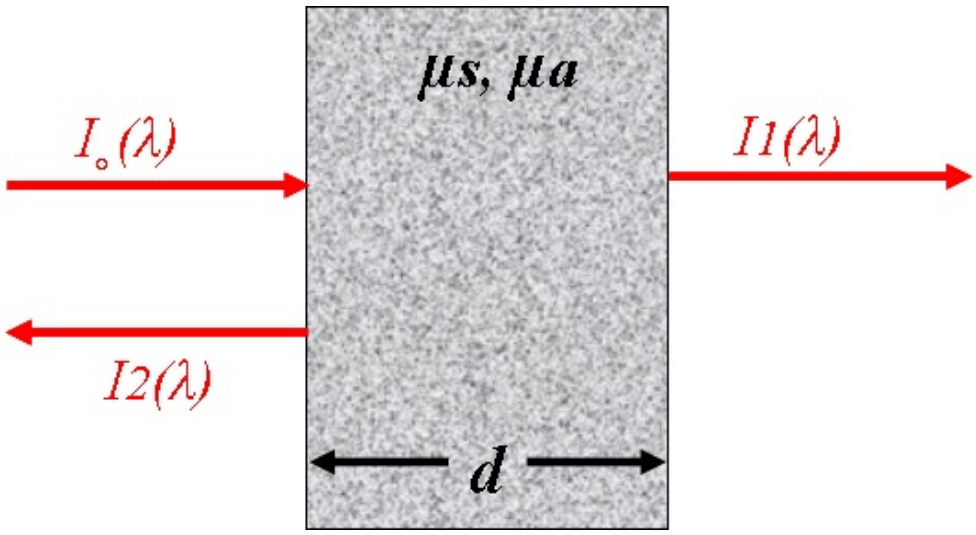

Figure 2.6: The incident light beam (I_0) is partly reflected (I_2), while passing (I_1) through the medium. The Beer-Lambert law states the relationship between the intensity of incident and reflected light.

traveled by the optical beam in the material. The intensity of light decreases exponentially with depth (d) in the material.

When light is reflected, the relationship between the intensity of the incident and the reflected beams is given by

$$I_2(\lambda) = I_0(\lambda)e^{-2d(\mu_s(\lambda)+\mu_a(\lambda))} \tag{2.2}$$

where μ_s and μ_a are scattering and absorption attenuation coefficients respectively. I_2 is the intensity of the reflected light after double passing through the device. The factor of 2 in the exponent explains the double pass of the beam through the material (Figure 2.6).

2.3.2 Attenuation

The objective of this thesis was to develop automatic image processing algorithms that would allow for precise extraction of the stromal attenuation coefficient from OCT images of human corneas acquired in-vivo. Furthermore, we wanted to measure in-vivo the time-dependent variability of the optical attenuation coefficient (scattering and absorption) of the human corneal stroma resulting from contact lens wear induced hypoxia. The stromal

attenuation coefficient can be measured by applying Beer-Lambert's law (Equation 2.2).

$$\mu(dB) = 10log_{10}\frac{I_0(\lambda)}{I_2(\lambda)} \tag{2.3}$$

Chapter 3

Background – Image Processing

In this chapter we review some of the basic concepts about image processing which are required to explain the proposed method in this thesis.

3.1 Image Segmentation

The goal of this research was to develop algorithms for segmenting the stroma, flattening of the cornea, compensation of the effect of the corneal curvature of the image SNR and contrast, as well as extracting the optical attenuation properties of the cornea from the OCT tomograms. We used the hypoxia data to be able to test how our algorithms perform under different conditions and can they provide statistically significant measure of the attenuation changes caused by the hypoxia.

Image segmentation [1, 32, 38, 43, 44] has numerous applications. Face recognition [52], fingerprint recognition [2], object location in satellite images [29] and crop disease detection in agricultural imaging [3] are some types of its usage. Using segmentation in medical imaging is one of the most important applications, such as tumor detection [61], tissue volume measurement [49] and study of anatomical structure [42]. Image segmentation has an essential role in the medical imaging field to find a specific object or area from an organ, for the purpose of matching, identification or investigation of changes in organs. Segmentation divides a digital image into several regions or objects to represent the image in meaningful interpretation. In general, image segmentation is used to find objects and boundaries and partitioned regions of interest from the rest of image. Two major types of image segmentation are fully-automatic segmentation and semi-automatic segmentation

[43]. Thresholding [64], edge detection [6], and region growing [70] are some common techniques which are used in any kind of segmentation.

Fully-automatic segmentation: This type of segmentation [23, 67] is completely unsupervised, this means that no initial point is needed to be defined by user to start the segmentaion. The processing speed of fully-automatic segmentation is fast and the results are accurate. Active contour model (snake) [23] is a sample of automatic segmentation which deforms a contour to lock onto features of interest within an image by means of energy minimization. For example in medical imaging this type of segmentation is used to find the brain contours [1] or leg bones [10] and provides some features like area, angles and length which helps doctors diagnose diseases.

Semi-automatic segmentation: In this kind of segmentation [66], the user specifies the region of interest and algorithms are only applied to that region to have the best segmentation. The user's selected region is a rough estimation of object contours, while semi-automatic segmentation method does accurate segmentation and finds the desired object contours precisely. The weakness of this kind of segmentation is the user's subjective factors which impact the original image [25, 34]; these factors also increase the operation time. The semi-automatic segmentation could be used on any image. There is an interaction between the user and the semi-automatic algorithm during the segmentation process so the algorithm takes advantage of user knowledge to have better segmentation. Semi-automatic segmentation can be used in other applications such as graphic art [31] or tumor identification in medicine [26, 30].

Several algorithms and methods have been developed for fully-automatic and semi-automatic segmentation. Edge detection [6], region growing [40, 62], are two methods of segmentation.

Edge detection: Edge detection is used to identify edges, which are the rapid changes in image intensity and usually related to the boundary of object in an image. Edge detection is a fundamental subject in image analysis. It has been used to identify the image boundaries. Edge detection is one of the most common techniques used in segmentation, feature extraction and feature detection. Two series of measurements exist to find edges (the sharp intensity changes) in the image. In the first measurement, the places where the first derivative of intensity is larger than a threshold are identified. In the second measurement, the places where the second derivative of intensity has a zero crossing are found. Several methods are used to detect the edges in an image, which are calssified to supervised and unsupervised methods, in the supervised method some primitive information are needed to detect the edges

(a) Original image (b) Canny detector [8]

Figure 3.1: Edge detection is a helpful image segmentation methods. Several methods are used to detect edges and the Canny edge detector is one of the famous operators in this area.

but in the unsupervised methods, such as Canny [8, 13], Sobel[28], Prewitt [19] edge detector, we don't need any information. Figure 3.1 shows the result of applying the Canny edge detector to the Lena image.

Region growing: In region growing segmentation [5, 70], a number of small primitive regions are chosen in an image, these small regions are called seeds. These seeds are assumed to be homogeneous. Then these regions are repeatedly merged together to create larger regions until any homogeneous region can't be made and all pixels of image are allocated to a region. The new region is created by comparing all unallocated neighboring pixels to the specific region. Some values have been acquired by calculating the difference between the unallocated neghboring pixel's intensity and region's mean. The unallocated pixels with the smallest differential value will be allocated to the corresponding region.

3.2 Image Enhancement

We need to enhance the image quality of corneal OCT images to increase the contrast, segment the cornea and flatten it to measure the stromal thickness with high precision and

also we need to compensate the effect of corneal curvature and focusing to calculate the total stromal attenuation coefficient.

The aim of image enhancement is to improve the image quality and perception of information to the viewer or to supply better input for other image processing purposes [35, 39, 50]. Image enhancement techniques are used to emphasize the image features representation and analysis. Removing blurring, enhancing contrast by using histogram equalization [69, 59], adjusting image intensity values and denoising are examples of enhancement operations. For example, an image might be taken of an endothelial cell, which might be of low contrast and somewhat blurred. Several methods exist to enhance the image such as noise reduction, the contrast range increment and blurring [39]. Figure 3.2 shows the results for some image enhancement techniques. The original image might have a broad range of intensity from very high to very low. Adaptive enhancement algorithms adjust their operation based on the image information (pixels) being processed. In this case the mean intensity, contrast, and sharpness (amount of blur removal) can be adjusted based on the pixel-intensity statistics.

The enhancement methods can be classified into two categories: spatial domain methods [57] and frequency domain methods [55]. In spatial domain methods we directly work on image pixels and manipulate them to get the proper enhancement. However, in frequency domain methods the image first is transferred to frequency domain, then enhancement applications are applied on transformed image and finally by using the inverse of transformation the enhanced image is provided.

3.2.1 Contrast

Contrast [11, 12] is a factor to distinguish objects in an image. In reality, contrast is the difference in the color and brightness between objects which has more impact than the brightness of object by itself due to human visual system mechanism. Contrast is the relationship between the distribution of color values in an image and the appearance of that image. Figure 3.3 shows an example of controlling the contrast of an image. The left image is the original image and the right image is contrast filtered and has higher contrast. Based on different situations various definitions of contrast exist. One of them is luminance contrast [41] which is defined as

$$C = \frac{\Delta L}{A_l} \tag{3.1}$$

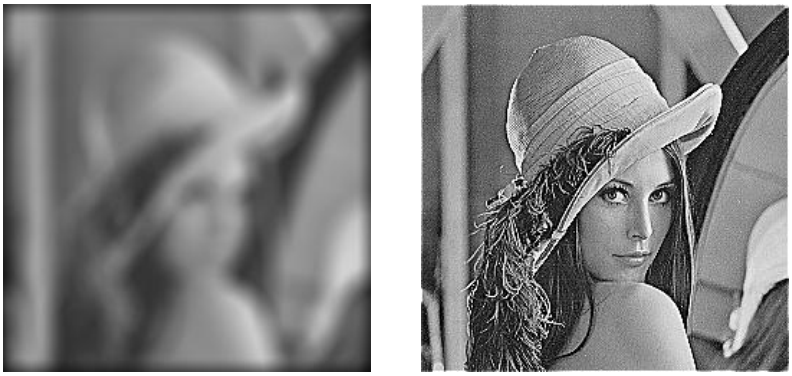

(a) Blurred (b) Deblurred

(c) Noisy (d) Denoised

(e) Lower contrast (f) Higher contrast

Figure 3.2: The quality of images are increased by using image enhancement techniques. These are some examples of image enhancement techniques. Left images are the modified images under some channel effects and the right ones are the recovered images by using image enhancement techniques such as deblurring, denoising and contrast enhancement methods.

where ΔL and A_l representing the luminance difference and average luminance. Weber contrast [41] is another common definition for contrast which is defined as

$$C_w = \frac{I - I_b}{I_b} \tag{3.2}$$

where I is the luminance of image and I_b is the luminance of background. This contrast is used in large uniform background with small features or symbols. Michelson contrast [33] is another common contrast which used for cases with similar bright and dark features and is defined as

$$C_m = \frac{I_{max} - I_{min}}{I_{max} + I_{min}} \tag{3.3}$$

where I_{max} and I_{min} are the highest and lowest luminance, respectively. Finally root mean square contrast [41] is defined as a standard deviation of the pixel intensities which is normalized in the range [0,1] and does not depend on the spatial distribution of contrast in the images.

$$C_{rms} = \sqrt{\frac{1}{MN} \sum_{i=0}^{N-1} \sum_{j=0}^{M-1} (I_{ij} - \bar{I})^2} \tag{3.4}$$

with I_{ij} representing the i^{th} j^{th} element of image with size $M \times N$ and $\bar{I}$ is the average intensity. The image I has a normalized intensity between 0 and 1.

Histogram Equalization

Histogram equalization (HE) is a contrast adjustment approach for image enhancement. HE can transform the intensity value to match with a predefined histogram [71] to increase the contrast of an image. It simply distributes intensities on the histogram to have an image with higher contrast. HE can be applied globally to the whole or a portion of the image. Figure 3.4 shows the original and the enhanced images by applying HE.

Let n_i be the number of occurrences of gray level i in image x:

$$p_x(i) = p(x = i) = \frac{n_i}{n},\ 0 \leq i < L \tag{3.5}$$

where L is the total number of gray levels in the image and n is the total number of pixels in the image with histogram $p_x(i)$ for pixel value i which is normalized between 0 and 1.

Cumulative distribution function is defined as:

$$cdf_x(i) = \sum_{j=0}^{i} p_x(j), \tag{3.6}$$

(a) Original image (b) Contrast filtered

Figure 3.3: Here we have an example of controlling the contrast, the contrast filtered image (b) has higher contrast than the original one (a).

where i is the pixel index, $p_x(j)$ is the corresponding distribution function and n is the total number of pixels in the image. In our approach, we are interested in a linear transformation T to map x to image y

$$cdf_y(i) = iK \tag{3.7}$$

$$y = T(x) = cdf_x(x) \tag{3.8}$$

where K is a constant and the transformation T maps the image to output range $[0, 1]$. We may need to use another mapping function to put in the image x histogram range:

$$y\prime = y \cdot (max\{x\} - min\{x\}) + min\{x\} \tag{3.9}$$

Histogram equalization is used in OCT images to incearse the image contrast to have better edge detection to find the layers in the cornea.

3.2.2 Morphology

Morphology [4, 22, 36, 54, 68] is a shape-based image processing technique to perform common tasks, such as contrast enhancement, noise removal, segmentation, etc. A function is applied to every pixel and its neighbours in the input image to find the corresponding

pixel in the output. The size and shape of neighbourhoods are the main parameters of this function to do morphological operations.

To analyze and process of geometrical structures, we employ mathematical morphology (MM) (i.e. set theory, lattice theory, topology, and stochastic process). It is usually applied to digital images but there is no limitation with graphs, meshes, solids and so on. MM includes a set of operations to transform discrete or continuous signals based on the defined characterizations. MM was developed [36] for binary images initially and then extended to gray scale ones [4], as well as complete lattices.

There are two different types of morphology: binary and grayscale morphology.

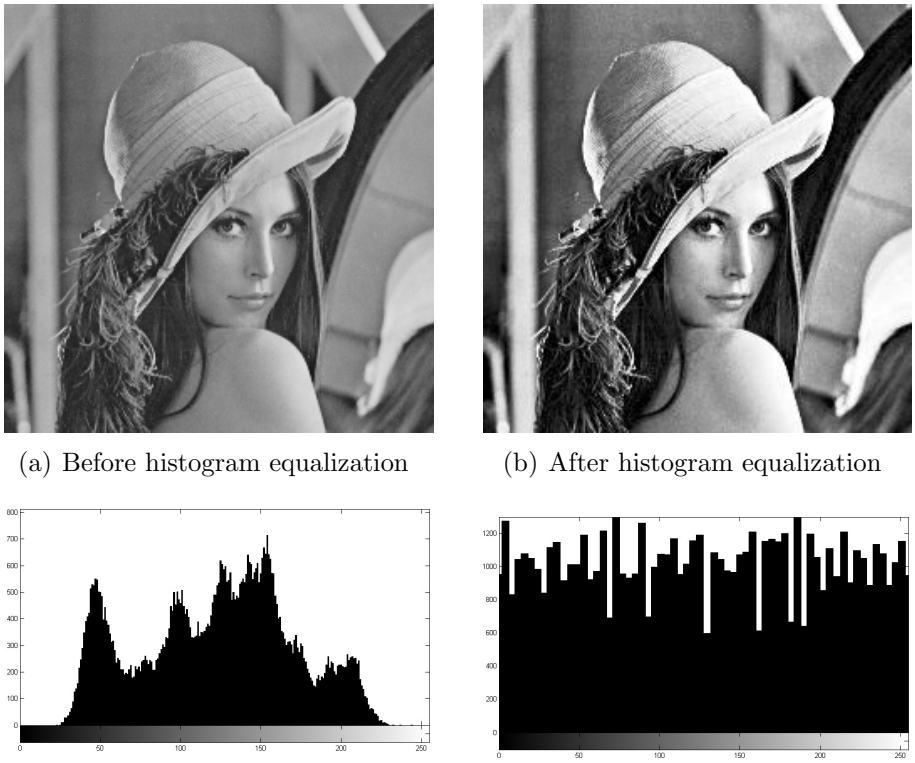

(a) Before histogram equalization

(b) After histogram equalization

(c) Histogram before equalization

(d) Histogram after equalization

Figure 3.4: The original image (a) has low contrast around the middle part of the intensity range (c), while the output image (b) intensities are distributed throughout the range (d) after histogram equalization

Binary Morphology

In this type of morphology, a signal is deemed a subset of an Euclidean space or the integer grid. The main goal is to find matching parts between the image and a template. This template is also called the structuring element which is a binary image. In binary morphology, erosion, dilation, opening and closing are the basic operations (all shift-invariant).

Grayscale Morphology

Grayscale morphology is simply a generalization of binary type that OR and AND operations are replaced with Max and Min operations. In this type, signals are being mapped to a set of reals $\mathbb{R} \cup \{\infty, -\infty\}$ where $\pm\infty$ are elements larger or smaller than any real number respectively.

3.3 Speckle Noise Reduction

Speckle noise is a random pattern that affects image intensity due to mutual interference of a set of wavefronts. It is a very important topic in the numerous applications such as laser based display systems. It is usually measured by the speckle contrast [9, 60]that its reduction is essential in many independent speckle patterns. Speckle noise reduction can be achieved by [60]

- Angle diversity: Illumination from different angles.
- Polarization diversity: Different polarization states.
- Wavelength diversity: destroy the spatial coherence.
- Moving or vibrating

OCT utilizes the spatial and temporal coherences of backscattered optical waves from biological tissue [15], which are subjected to presence of speckle noise. Speckle in OCT tomograms is dependent on both beam wavelength and object structure [45, 46, 51].

Therefore speckle includes morphological noisy object that the noise component defines granularity of the OCT image. Speckle noise obscures low frequency features in OCT images and degrades their quality. It also degrades the performance of algorithms that are

used to extract, analyze and diagnose the relevant features. As noise and signal separation is difficult in the OCT images, developing a successful speckle noise reduction is a real challenge. We try to reduce the speckle noise in OCT images by developing an algorithm.

Chapter 4

Problem Formulation

In this thesis, our goal is to develop novel image processing methods, specifically designed for high resolution OCT tomograms of the human cornea imaged in-vivo, that would permit measurement of the time-dependent variability of the optical attenuation coefficient (μ) of the human corneal stroma resulting from contact lens wear induced hypoxia. A complete set of human corneal images was provided by Dr. Bizheva's research group. The images were acquired in-vivo from eight healthy volunteers during a hypoxia study. Ten 2D images were recorded from approximately the same location in the cornea from all volunteers under normal conditions (baseline data). Afterwards, a soft contact lens was placed on the cornea of each volunteers and their eyes were patched to prevent normal oxygen delivery to the cornea for a duration of three hours. OCT images were recorded again immediately after the contact lens removal at three hours and later on every 15 minutes for a duration of two hours. Image analysis revealed that as expected, different layers of the cornea swelled over time because of water in-flux due to the hypoxia during the contact lens and eye patch wear. Later on, the cornea returned to normal state over a period of 2 hours after the lens and eye patch removal. The purpose of this study was to investigate how the stromal attenuation coefficient changes with hypoxia and if those changes correlate with the corneal swelling. But some problems exist which have to be solved before finding the attenuation. Several factors may have affected the precision of the extracted total attenuation coefficient. For example, spatial variations of the image contrast of corneal tomograms related to the natural curvature of the cornea affect the attenuation values and another factor is the focusing of the imaging beam. By looking at the corneal image in Figure 4.1, it is clear that the intensity (I) is maximized towards the middle of the cornea, both because of spatial variations in the illuminating beam, and possibly also because of corneal curvature.

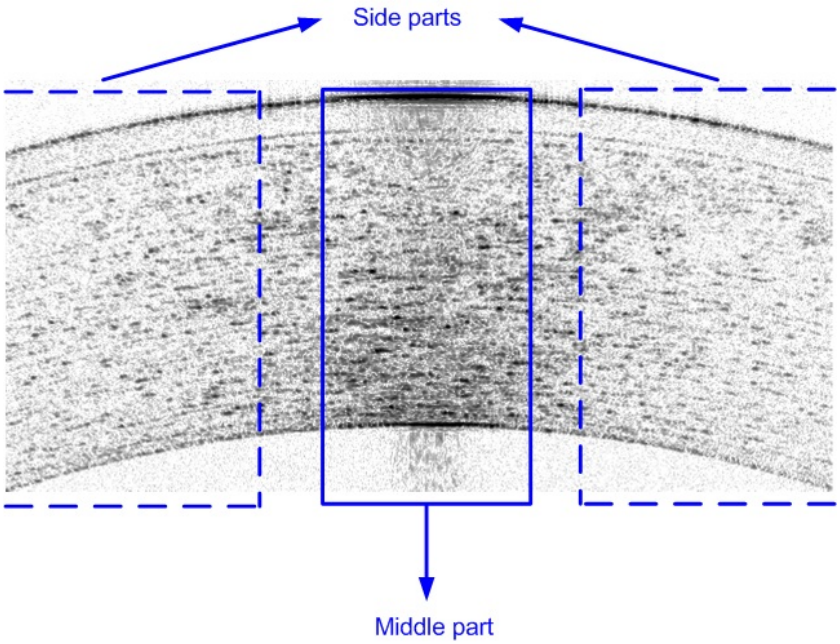

Figure 4.1: OCT corneal image of one individual. The backscattering phenomenon and focal point position in light beam lead to non-uniform illumination in corneal image; the middle part of image is darker than two sides. These analyses are based on image representation.

In this chapter, first we explain how create the **database**, then explain how **hypoxia** and **corneal curvature** affect attenuation coefficient values. After that, we explain how **attenuation coefficients** are corrected by considering **SNR variation** and **focusing correction** which affect μ values.

Dataset

We have used a database of OCT corneal images [17]. For each of eight individuals, an initial baseline set of ten images were taken, followed by placing a soft contact lens (SCL) over the eye to induce corneal edema (swelling from water intake). Then the eye was patched for three hours. Following the removal of the lens, a set of ten images was acquired every 15 minutes over a period of two hours. So for each individual we have 13 time steps (WO, WL, M1, M2, ..., M11) and in each time step a set of ten images exists. Figure 4.2 shows the OCT corneal results for one individual before using contact lens (WO), immediately after contact lens removal (WL) and 15 minutes after contact lens removal

(M1). Some of the OCT images are not valid; a few of them have low resolution and are not suitable for evaluation. Some images are invalid because the subject has blinked during the OCT imaging so these corrupted images with eyelash artifacts are removed from the processed data.

Hypoxia

The purpose of this study is to assess the corneal response to hypoxia (lack of oxygen). Prolonged contact lens wear causes hypoxia in the human cornea that results in changes of the overall thickness of the cornea and the optical clarity. Hypoxia induced corneal thickness changes have been observed and quantified with an OCT system and an automatic segmentation algorithm [1, 10, 23]. Corneal clarity can be quantified by the use of optical scatter, absorption or total attenuation metrics. We expect to have a uniform illumination in the cornea before and after removing the lens, but Figure 4.3 depicts a corneal thickness (d), amount of water and clarity of specific individual were changed before (WO) and immediately after removing the contact lens (WL) which was worn for three hours. This phenomenon is very important since corneal thickness has influence on attenuation coefficients based on Beer-Lambert law equation in the section 2.3.1. The image contrast can be affected not only by the swelling of the cornea, but also by the location in the cornea the image was acquired from, since the image contrast is strongly dependent on the corneal curvature.

Curvature problem

After choosing the database, and considering the effect of hypoxia, we need to straighten the images and remove the corneal curvature to measure the stromal thickness, so an automatic algorithm is developed to remove the curvature and straighten the corneal image in Section 5.1.

Attenuation correction

The stromal attenuation coefficient (μ) is calculated using Beer-Lambert's law, which has been explained in Section 2.3.1. The attenuation coefficient is related to the incident light beam and reflected light (refer to Figure 2.6). We need to enhance the straightened corneal image and compensate the focal effect to have a meaningful comparison in the assessed attenuation for different images. Also, some analysis is required to correct for focus phenomena.

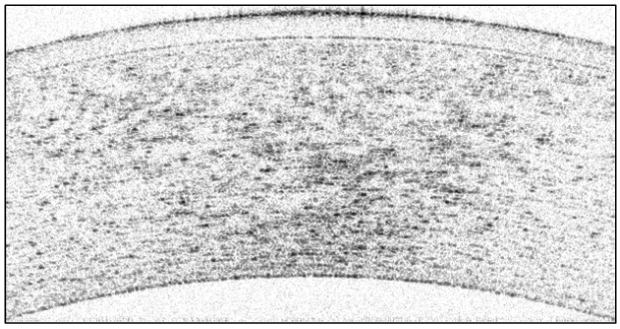

(a) Corneal image before contact lens

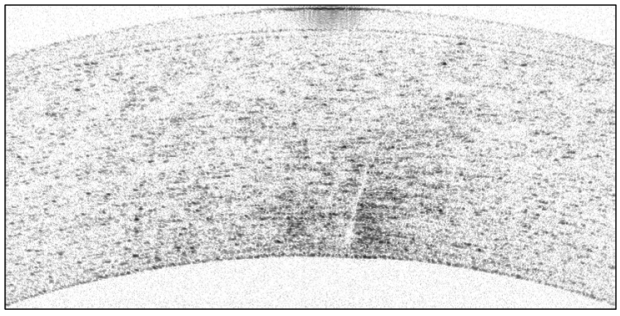

(b) Corneal image immediately after removing the contact lens

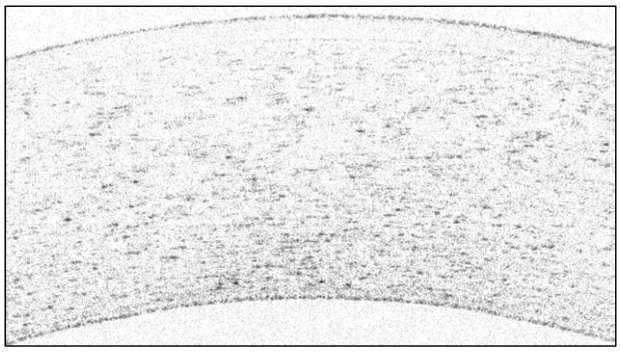

(c) Corneal image 15 minutes after removing the contact lens

Figure 4.2: Variations in OCT corneal images of one individual before (a) and after removing contact lens (b), (c)

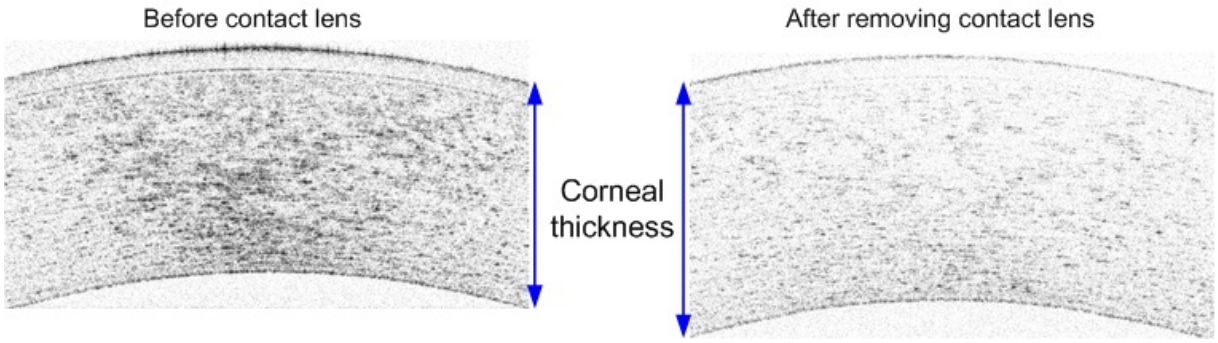

Figure 4.3: The left OCT image shows the OCT corneal image of a specific individual before contact lens wear. The right OCT image shows the OCT corneal image of same individual immediately after removing a contact lens which was worn for three hours. The corneal thickness and clarity have changed.

After the corneal image has been straightened, attenuation is measured. We expect to have positive attenuation coefficient (μ), but in some cases μ is negative which is impossible and due to two major factors: SNR variation over the scanning range of the OCT system, and the relative position of the focal plane of the optical beam with respect the front or back surface of the cornea. Therefore we have designed and applied SNR correction and focus correction procedures to the original data.

SNR variation

The SNR properties of an SD-OCT system affects imaging and intensity values of the corneal system. Since any changes in intensity values impress attenuation coefficients (μ), we have to find a solution to correct the intensity values (I_r).

Focusing correction

To have a precise measurement, we need to make sure that our imaging is accurate. Figure 4.1 shows a sample of the corneal OCT image with brightness variations from the top to the bottom of the image. The illumination is not uniform and the middle part of this image is darker than the side parts. The illumination variation in horizontal direction is due to the corneal curvature and the illumination variation in vertical direction is due to the focusing effect. During imaging, although we can not precisely set the position of the focal beams, we tried to adjust the focal point at the bottom of cornea (endothelium) with

maximum curvature to have minimum distortion. Due to the backscatter phenomenon, when light goes straight through the middle part of cornea (with maximum curvature) and slantwise on its sides, the corneal OCT image has the maximum illumination — due to maximum reflection — in the middle and minimum one in the sides. The apparent brightness of the outside of the cornea (top part of the measured image) relative to the inside (bottom) is greatly impacted by the focus behaviour of the instrument. That is, there appear to be variations in the degree to which the illuminating beam is focused, which induces variations in brightness quite unrelated to the cornea itself.

Chapter 5

Proposed Method

Prolonged contact lens wear causes hypoxia [58] in the human cornea that results in changes of the overall thickness and transparency of the cornea. Hypoxia induced corneal thickness changes have been observed and quantified with an ultrahigh resolution optical coherence tomography (UHR-OCT) system and an automatic segmentation algorithm [17, 21]. The objective of this thesis was to develop novel image processing algorithms that will allow for precise measurement of the corneal stroma attenuation coefficient from high resolution OCT images acquired in-vivo. As a result, stromal part extraction is a necessity.

2D UHR-OCT tomograms of the human cornea were acquired from eight healthy subjects. All measurements were conducted with the approval of the Human Ethics committee at the University of Waterloo. The 2D tomograms dimensions are 1000×512 (A-scans $\times$ pixels in depth). The UHR-OCT system was used to image the in-vivo human cornea with 3.2 μm axial and 10 μm lateral resolution in non-contact lens wearers. Corneal edema was induced by inserting a thick, soft contact lens (SCL) and patching the eye for three hours. A set of ten corneal images were acquired prior to insertion, immediately after the removal of the SCL, and subsequently every 15 minutes for two hours. The purpose of the study is to assess the corneal response to hypoxia (lack of oxygen).

First, we manually remove any corrupted images, e.g. with eyelash artifact, from the database. Then – as we will describe later in this chapter – the remaining corneal OCT images are segmented by morphological operators, and then they are straightened to measure the stromal thickness. The spatial variations in image contrast due to corneal curvature and laser beam focusing issue are also compensated to have uniform variation in image intensity. The stromal optical attenuation coefficient is derived through a statistical analysis via linear regression on averaged log intensity image data.

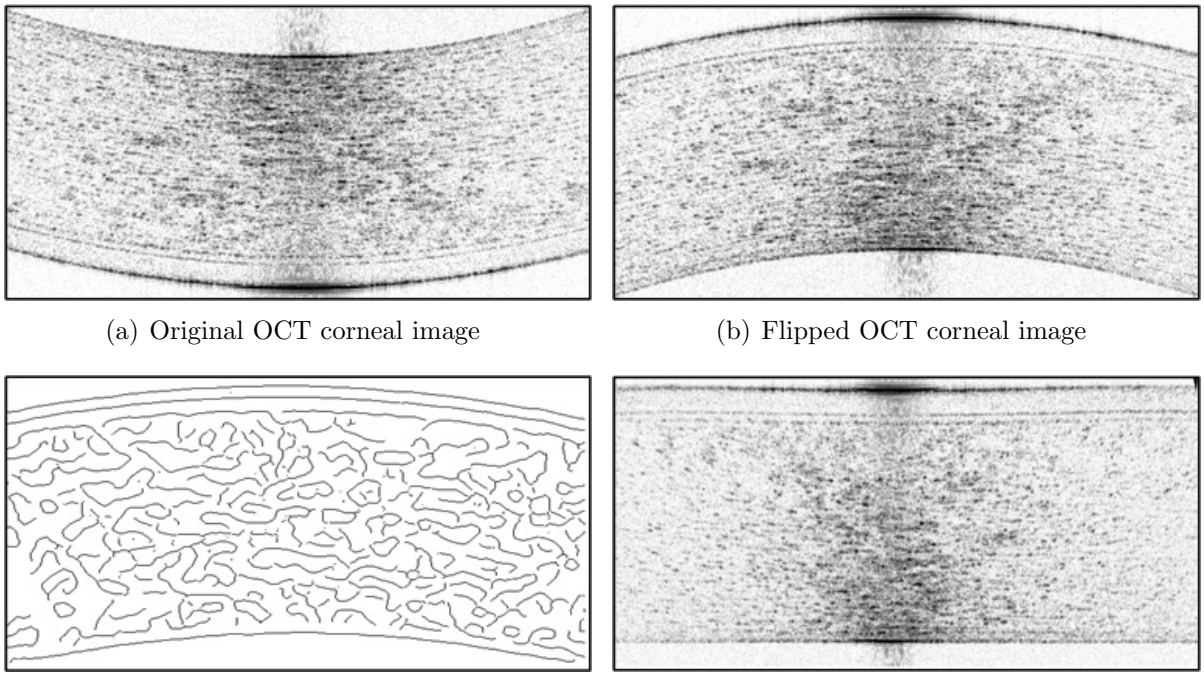

(a) Original OCT corneal image

(b) Flipped OCT corneal image

(c) Automatic morphological edge detector

(d) Flattened OCT corneal image

Figure 5.1: We need to use an automatic segmentation algorithm to segment the corneal image. The corneal image is flattened based on the curvature of the epithelium boundary, which is the toppest curve in (c).

5.1 Corneal Segmentation and Flattening

In this section, we briefly explain automatic corneal segmentation to extract the stroma. Some of the previous work [7, 17, 27] used a semi automatic segmentation algorithm [25, 34] to segment the corneas, but in this thesis a corneal flattening has been achieved by segmenting the high-contrast epithelium layer and shifting each column of image pixels to straighten the epithelium layer. In this research, we use an unsupervised morphological edge detector (explained in Section 3.1) to find the epithelium layer (see Figure 2.1(b)) with a thresholding which is set by user. After that, by using the epithelium layer's curve, the corneal image is flattened. Figure 5.1 shows a representative 2D UHROCT tomogram (1000 A-scans $\times$ 512 pixels), acquired from a healthy cornea in-vivo (5.1(a)) [17, 7]. The images are flipped, to have the corneal epithelium on top (5.1(b)). All corneal layers: the epithelium, Bowmans membrane, stroma and endothelium-Descemets complex, are

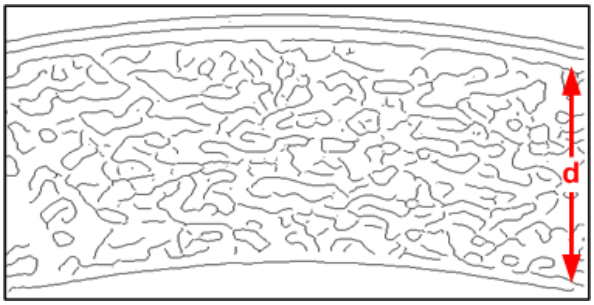

Figure 5.2: Stromal thickness – the distance d between inner boundaries at the top and bottom of the segmented image in Figure 5.1(c).

clearly visualized. We extract the epithelium layer by using the Canny edge detector and morphological operators such as erosion to be employed in the corneal image flattening; Figure 5.1(c) shows the result of epithelial boundary detection. Then based on epithelium boundary which is extracted from the segmentation phase, pixels in the image column are shifted up until the epithelium curvature is removed and straightened. The cornea is straightened since all layers in cornea are parallel; the flattened image is shown in Figure 5.1(d).

5.2 Stromal Thickness

Refering to Beer-Lambert law definition in the section 2.3.1, we can see that the stromal thickness (d) is necessary to calculate the total attenuation coefficient (μ).

$$\begin{aligned} I_2(\lambda) &= I_0(\lambda)e^{-2d(\mu_s(\lambda)+\mu_a(\lambda))} \\ \mu(\lambda) &= \mu_s(\lambda) + \mu_a(\lambda) \end{aligned} \tag{5.1}$$

The extracted stromal boundaries in the segmentation phase are used to find the stromal thickness (d) which is defined as the distance between the inner boundaries at the top and bottom of the corneal image (Figure 5.2).

5.3 Stromal Intensity properties

To have a precise attenuation coefficient measurement (μ), we need to make sure that the imaging was done accurately, so we need to remove all blinked or blurry images from

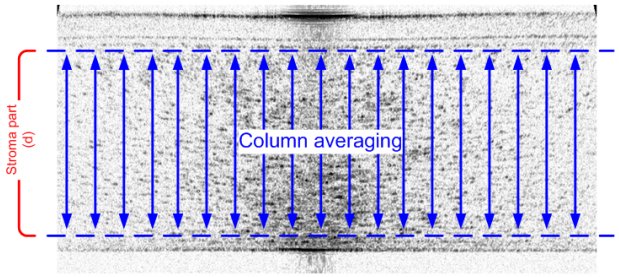

(a) Column intensity averaging concept

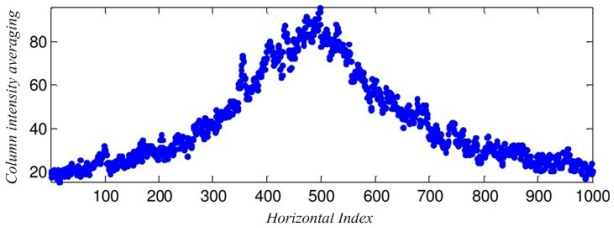

(b) Column intensity averaging results

Figure 5.3: Column intensity averaging of the stromal part of the straightened corneal OCT image. The blue dots in (b) correspond to column averaging values (a). Spatial variations in stroma brightness are attributed to spatial variations in the backscatter behavior; our goal is to use these variations in order to infer variations in the underlying anatomy.

the database. Figure 4.1 on page 22 has shown a sample of an OCT corneal image with brightness variations. The illumination is not uniform and the middle part of this image is darker than the sides. The middle part of the corneal image around the maximum point (zero gradient) of the boundary curve has the maximum illumination and the minimum illumination in the sides. The image contrast changes in horizontal direction because of the corneal curvature. The illumination changes in vertical direction because of the focusing effect of the imaging beam. The apparent brightness of the outside of the cornea (top part of the measured image) relative to the inside (bottom) is greatly impacted by the focus behaviour of the instrument. That is, there appears to be variations in the degree to which the illuminating beam is focused, which induces variations in brightness quite unrelated to the cornea itself.

To see the backscatter behavior, we have acquired the column averaging along corneal stroma (Figure 5.3(a)) toi find the the intensity variation by using the following equation

$$I_c(i) = \sum_{j=d} I(i,j), \tag{5.2}$$

where $I_c(i)$ is the column intensity averaging over the stromal part with thickness d and $I(i,j)$ is the intensity value of each pixel in a corneal image. To find $I_c(i)$ we have to know the exact thickness of stroma (d).

Figure 5.3(b) shows the corneal spatial column intensity averages of the straightened corneal stroma in the OCT image. It shows the stromal intensity, with spatial intensity averages shown for the outside (image top) and inside (bottom) parts of the stroma. It is obvious that the maximum image intensity occurs in the middle of the cornea, because of fluctuations in the illuminating laser beam, and the corneal curvature itself.

Figure 5.4(a) shows the stromal part of flattened corneal image; Figure 5.4(b) and 5.4(c) show the column averaging intensity of 50 rows on top and bottom of stroma calculated by equation 5.2.

The bottom segment of image (50 rows at the bottom) has much higher brightness than top part (50 rows at the top) with a bell-shape spatial distribution and a noticeable peak in the middle of intensity. We expect to have uniform distribution of intensities at the top and bottom of image since there isn't any difference between top and bottom of cornea. Calibration issues; i.e. beam focusing and channel physical properties; i.e. corneal curvature may cause this distortion.

Figure 5.5 shows the column intensity averaging result of stroma for a specific individual before using contact lens (WO), with contact lens (WL) and after removing the contact lens (M1). The intensity distribution and the maximum intensity value vary between time steps (WO, WL, M1, ..., M11).

5.4 Stromal Attenuation Coefficient

The stromal attenuation coefficient (μ) is calculated by using Beer-Lambert's law, which is explained in the section 2.3.1. Attenuation coefficient can be measured by measuring the row intensity averaging (Figure 5.6).

$$I_r(j) = \sum_{i=1}^{1000} I(i,j), \tag{5.3}$$

where I_r is the row intensity averaging over the width of a corneal image (1000 pixels) and $I(i,j)$ is the intensity value of each pixel in corneal image. The attenuation coefficient (μ) is calculated by using the row intensity average and it is based on Beer-Lambert law

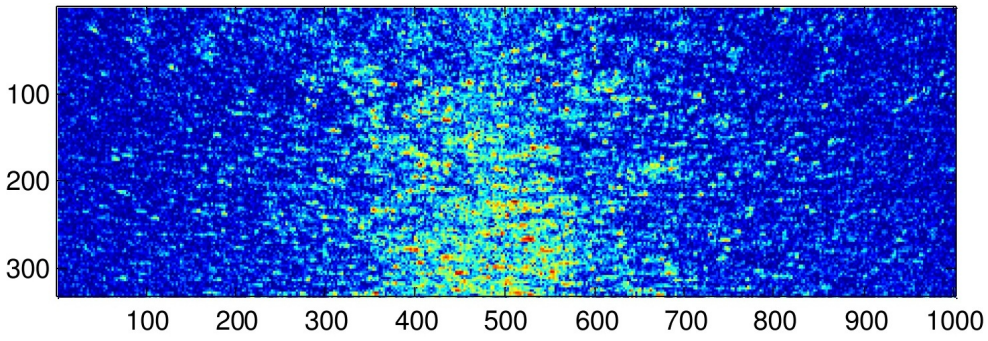

(a) Straightened stroma

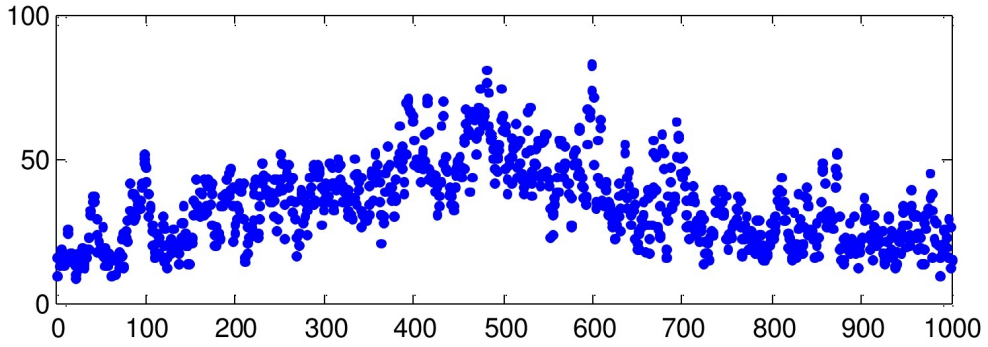

(b) Column intensity in top part of stroma

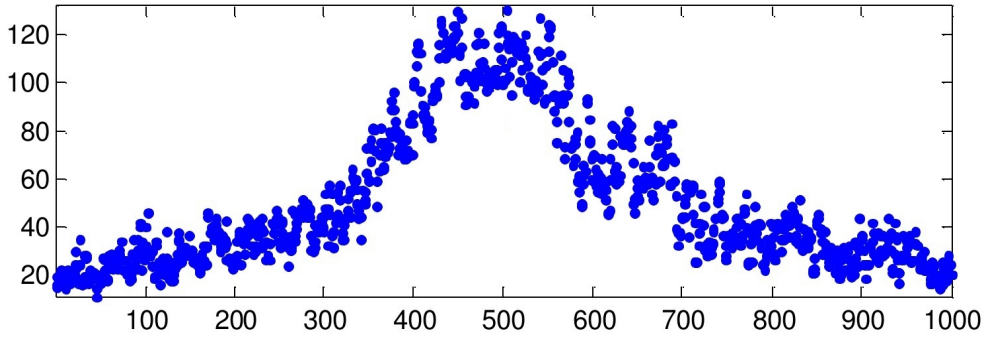

(c) Column intensity in bottom part of stroma

Figure 5.4: Spatial variations in stroma brightness attributed to spatial variations in the backscatter behavior; our goal is to use these variations in order to infer variations in the underlying anatomy (refer to Figure 5.3).

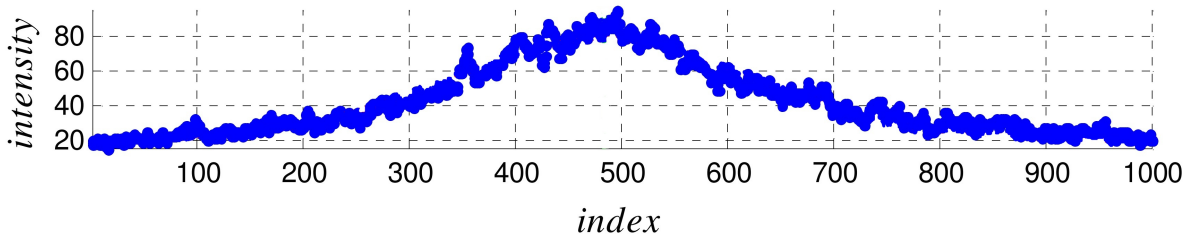

(a) Stromal column intensity before contact lens wear

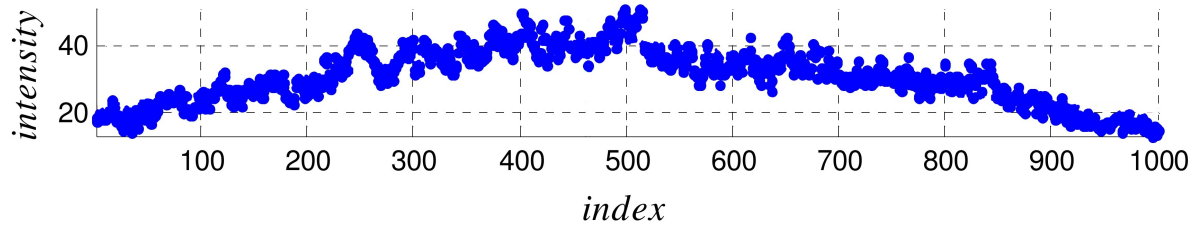

(b) Stromal column intensity immediately after removing contact lens

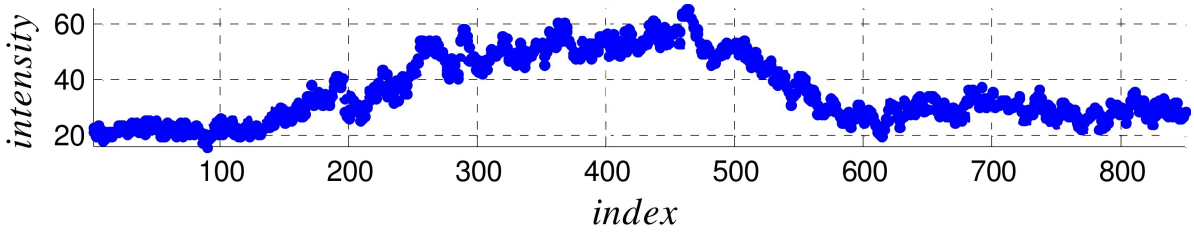

(c) Stromal column intensity 15 minutes after removing contact lens

Figure 5.5: Column intensity averaging before (a), immediately after removing the contact lens (b) and 15 minutes after removing contact lens. We can see the intensity values have changed over time. We want to compare these variations over all time steps.

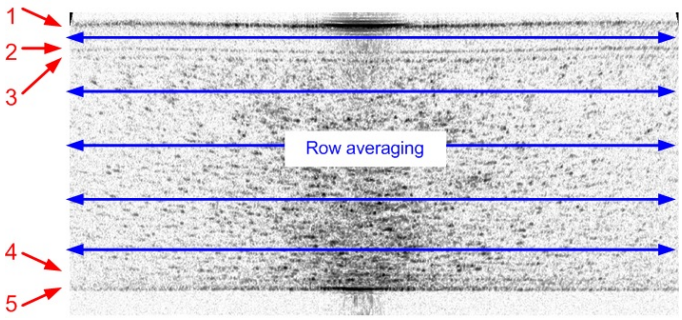

(a) Row intensity averaging concept

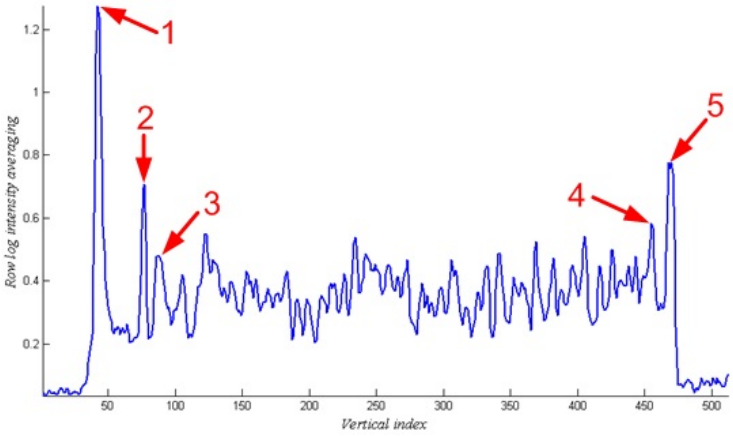

(b) Row intensity averaging results

Figure 5.6: Row intensity averaging of stroma part of straightened corneal OCT image. The numbers in (b) are corresponding to different layers in (a).

equation (2.1)

$$\mu = -\frac{\log I_r}{2d} \tag{5.4}$$

where $\log I_r$ is logarithmic row intensity averaging of the corneal image shown in Figure 5.6(b) and d refers to the stromal thickness.

We compute the attenuation coefficient by finding the best fit line to the stroma (log-intensity between 3 and 4 in Figure 5.6(b)) with two methods which are shown in Figure 5.7. In the first method, we find the best fit line to logarithmic row intensity averaging values $\log I_r$ (blue dots). In the second one, we apply a histogram equalization algorithm [69, 59] to $\log I_r$ and get new values (black dots). Now, we have found the best linear fitting coefficients in the presence of noise and artifacts for evaluation of the individual's

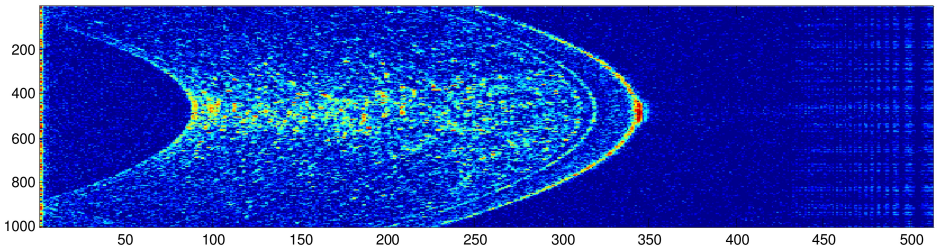

(a) Corneal image - Patient 1

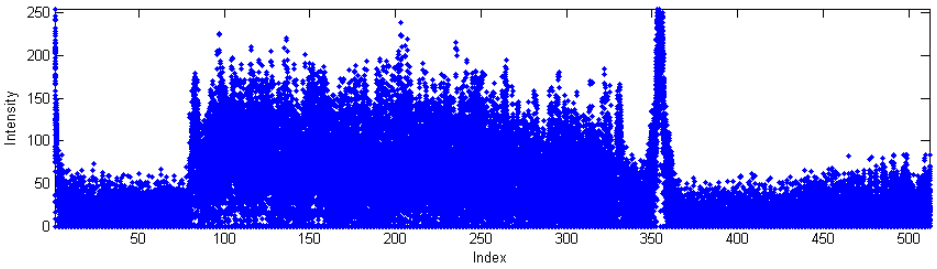

(b) Intensity of cornea - Patient 1

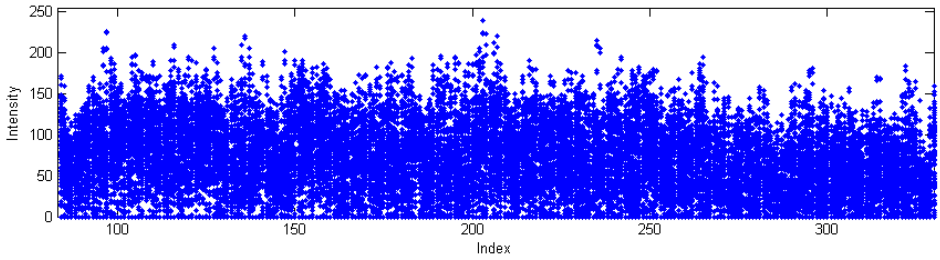

(c) Intensity of stroma - Patient 1

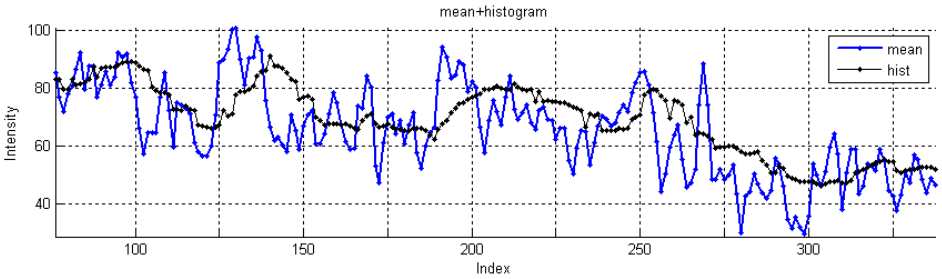

(d) Row intensity averaging - mean vs. histogram method

Figure 5.7: Finding the best fit line to logarithmic averaged intensity in stroma to find the attenuation coefficient. This fitting can apply to an averaged intensity (blue dots in 5.7(d)) or a histogram equalized data (black dots in 5.7(d)) to have an acurate fitting line.

stromal attenuation. The stromal optical attenuation coefficient is quantitatively assessed via linear regression analysis on the log-intensity data averaged over a single image. We use histogram equalization method to find better fitted line to $\log I_r$ to compensate the curvature problem in the stroma and acquire the attenuation value.

The regression analysis is intended to detect the exponential decay in brightness due to corneal backscatter, however the difficulty in a straightforward regression analysis is that, in addition to the backscatter phenomenon, the apparent brightness of the outside of the cornea (top part of the measured image) relative to the inside (bottom) is greatly impacted by the focus of the instrument. That is, there appears to be variations in the degree to which the illuminating beam is focused, which induces variations in brightness quite unrelated to the cornea itself. Therefore, to have a meaningful comparison in the assessed attenuation for different images, some analysis is required to correct for focus phenomena.

Regression analysis is a statistical model for the investigation of the relationship between dependent variables and one or more independent variables. The goal of regression analysis is to determine the values of parameters for a function which is the best fit for a set of provided data. In linear regression, the function is a linear equation.

Figure 5.8(a) shows a representative 2D UHR-OCT tomogram (1000 columns $\times$ 512 pixels), acquired from a healthy cornea in-vivo. The cornea consists of four layers (the epithelium, Bowmans membrane, stroma and endothelium-Descemets complex) which are clearly visualized. Figure 5.8(b) depicts a flattened 2D UHROCT image of the human cornea and a logarithmic intensity value average over 100 columns in the center (apex) of the flattened corneal image (red rectangle) has been shown in Figure 5.8(c). The flattening has been achieved by the method explained in Section 5.1. Only 100 columns in the center of the image (red rectangle) are selected because the maximum intensity is located in the middle of the image and the intensity is reduced at the sides. Figure 5.9 shows the way that attenuation coefficient (μ) has been calculated. First the row intensity averaging is computed (Figure 5.9(a)), then its stromal region has been selected (Figure 5.9(b)) and finally a line has been fitted to this curve (magenta dashed line in Figure 5.9(c)) to find the attenuation coefficient.

We expected to see a negative slope in stroma part (curve between 3 and 4 of row intensity averaging result in Figure 5.6(b)) due to the progressive loss of light from scattering and absorption in the cornea. Instead, in some cases a positive slope was observed due to SNR variation over the scanning range of the OCT system, and the relative position of the focal plane of the optical beam with respect the front or back surface of the cornea. Therefore we have designed and applied SNR correction and focus correction procedures

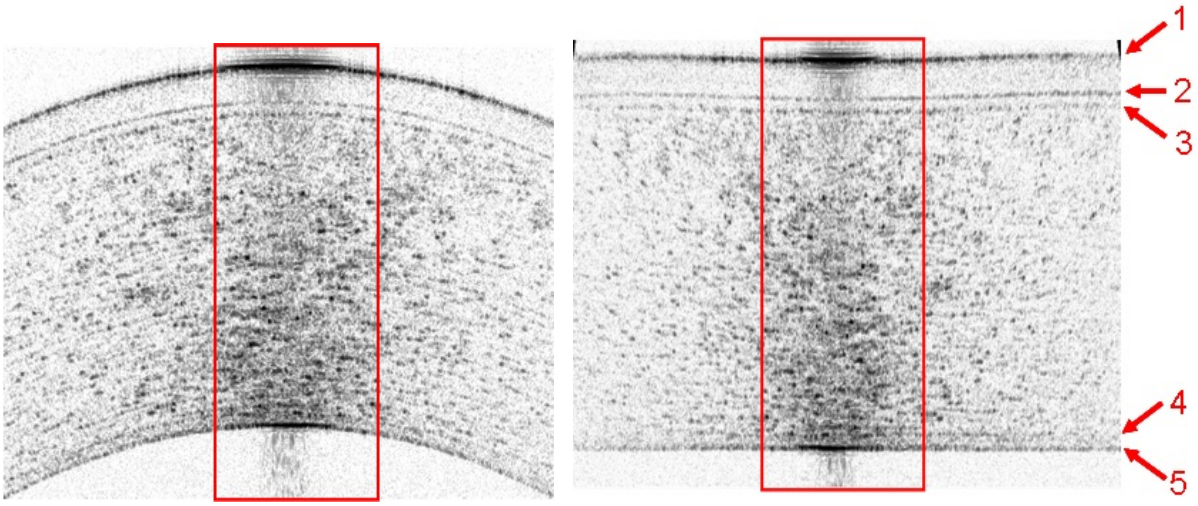

(a) Original image

(b) Flattened image

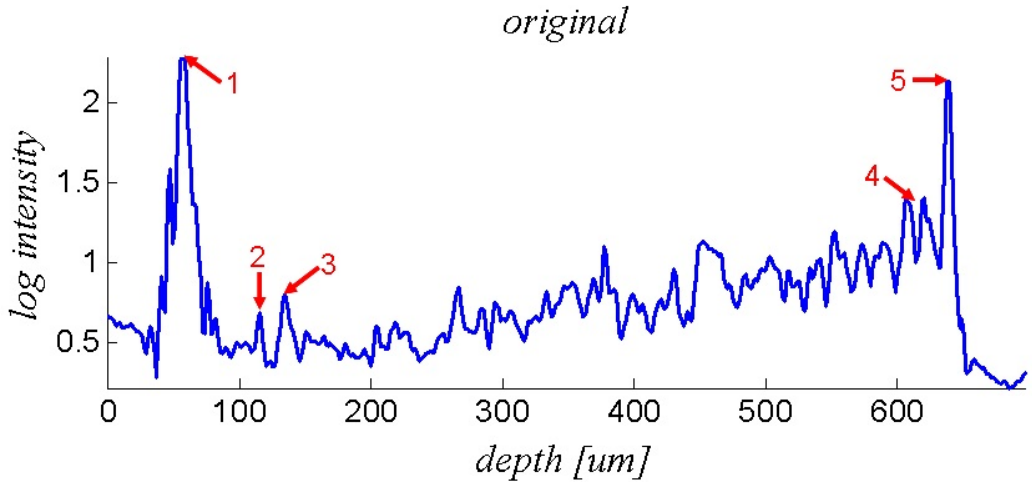

(c) Logarithmic intensity values of row intensity averaging in the middle of the flattened image

Figure 5.8: A representative 2D UHR-OCT tomogram (1000 columns × 512 pixels), acquired from a healthy cornea in-vivo (a). All corneal layers: the epithelium, Bowmans membrane, stroma and endothelium-Descemets complex, are clearly visualized. A representative flattened 2D UHROCT image of the human cornea (b), and a logarithmic intensity value average over 100 columns in the center (apex) of the flattened corneal image (red rectangle) (c).

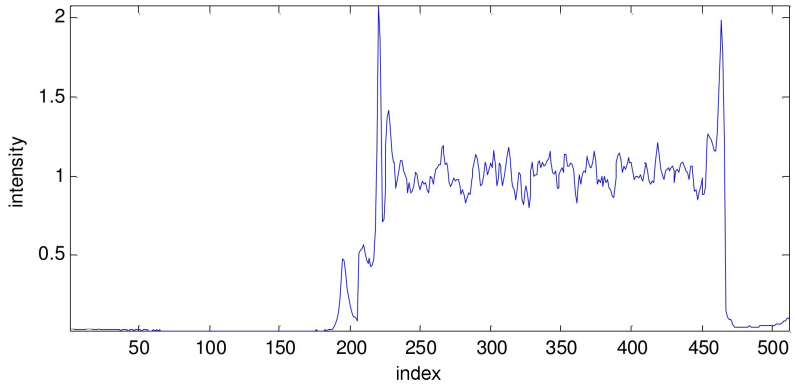

(a) Row intensity averaging

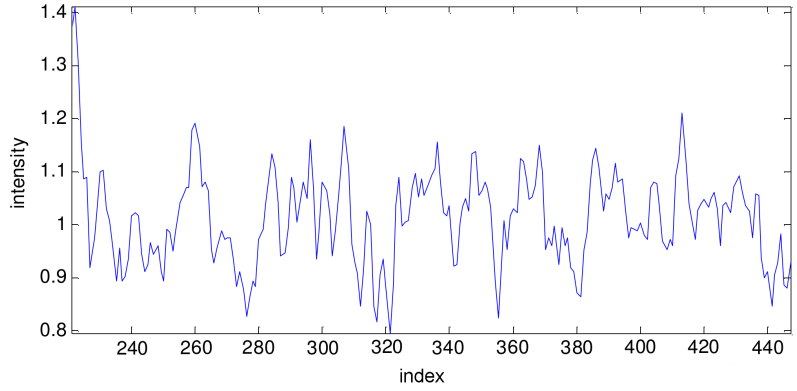

(b) Row intensity averaging in stromal region

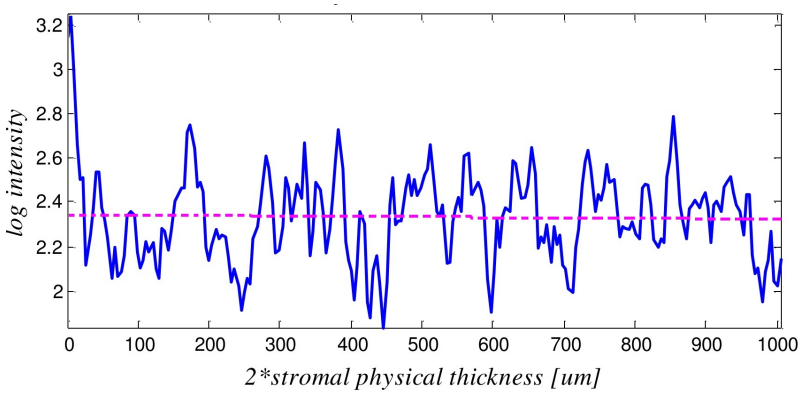

(c) Row intensity averaging in stromal region in μm domain and linear curve fitting to determine the attenuation coefficient (μ)

Figure 5.9: An attenuation coefficient is computed by finding the slope of stromal region of row intensity averaging results

to the original data (Section 5.4.1 and 5.4.2) .

5.4.1 SNR Correction

Figure 5.10 shows the SNR of the SD-OCT system measured with a mirror (blue bubbles) corresponding to propagation channel effect in the communication system. This effect must be compensated (equalized) before attenuation coefficient extraction. A parabolic curve is fitted to extract the intermediate pixels other than measured SNRs. To compensate the noise effect, the inverse of SNR values (channel coefficients) are applied to the row averaged intensities (I_r) of the flattened cornea. Figure 5.11 shows the row averaged intensities after equalization. The flattened cornea before and after SNR correction have been depicted in Figure 5.12; a uniform distribution of compensated intensity signal results in the extraction of attenuation coefficient (μ).

SNR measurement was measured only one time after hypoxia study, and We are not make sure that the setting and measurements are the same during the whole process; therefore, this phase correction is left out from corrections.

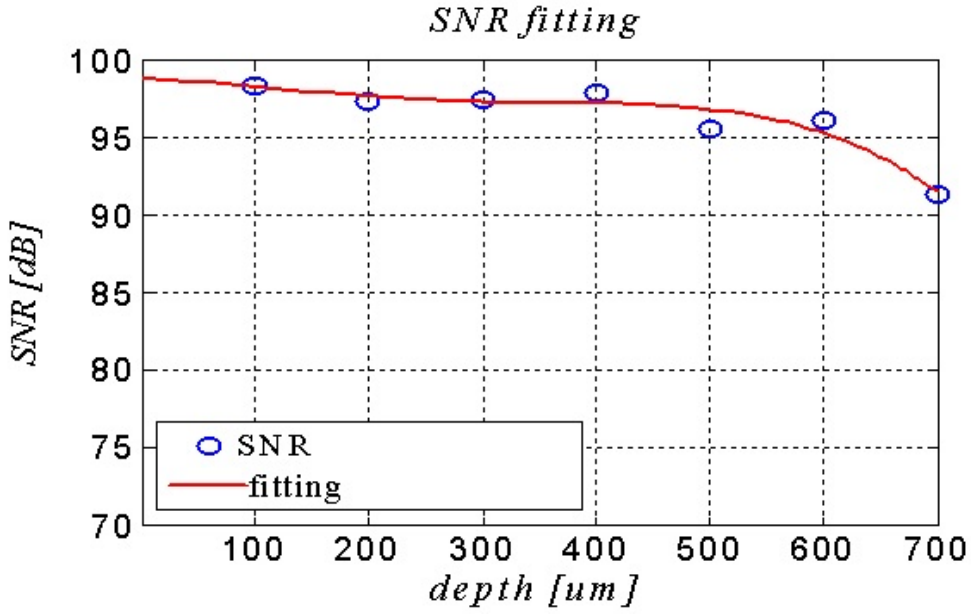

Figure 5.10: SNR of SD-OCT system measured with a mirror for SNR compensation to prevent the probable positive slope in I_c, e.g. Figure 5.8(c).

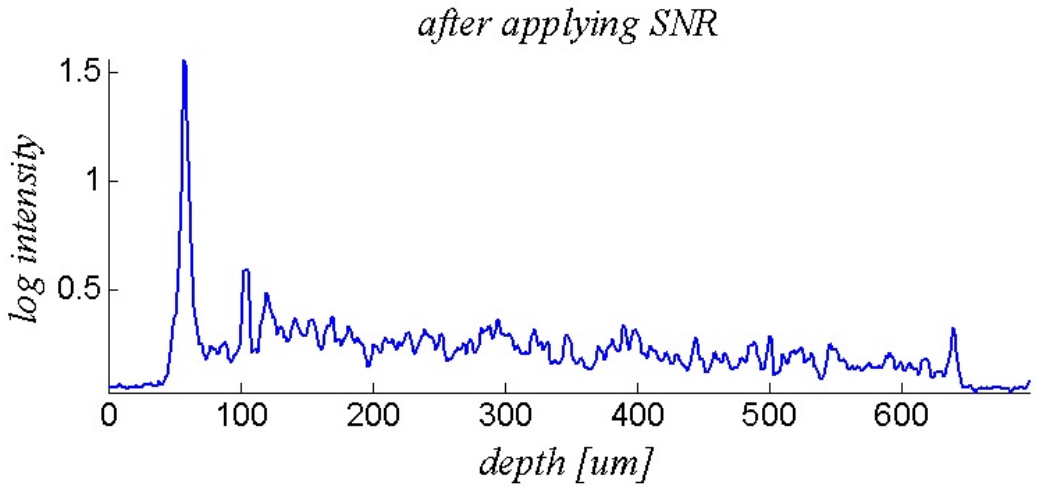

Figure 5.11: Logarithmic row intensity averaging result for patient 1 after applying SNR correction to Figure 5.8(c).

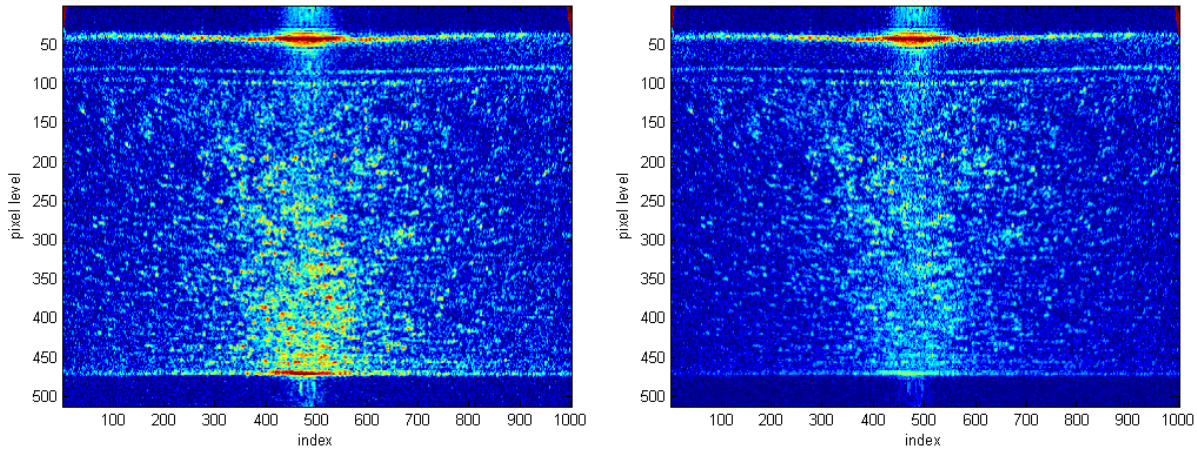

(a) Original flattened image before SNR correction (b) Flattened corneal image after SNR correction

Figure 5.12: Flattened corneal image before (a) and after (b) applying SNR correction in Figure 5.10.

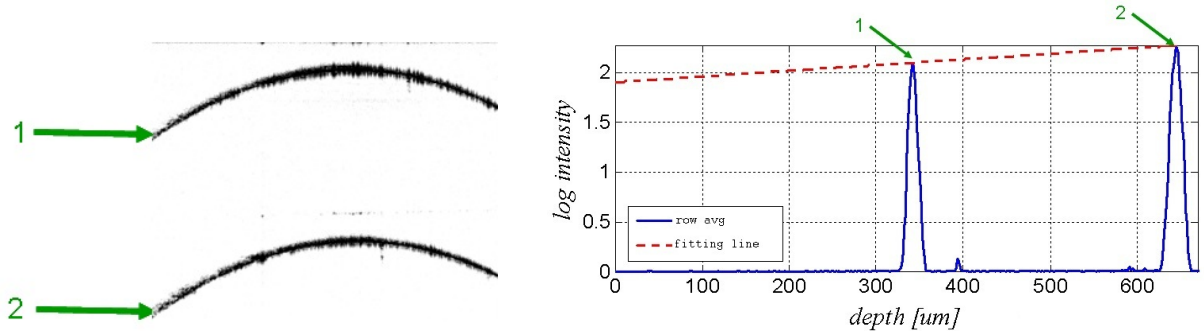

(a) OCT image of clear glass lens; two curves corresponding to theedges of a glass lens

(b) Row intensity averaging result of glass lens

Figure 5.13: A clear glass contact lens (a) is used to compensate the focal point problem. Since it has been made from glass, the backscattering and absorption phenomena will not exist in OCT imaging. We expect to have same peaks at sides of glass lens but two different peaks have been observed since the beam is focused on the back side of the glass lens (b).

5.4.2 Curve and Focus Correction

Several factors affect the precision of the extracted total attenuation coefficient. One of them is the contrast spatial variation in corneal tomograms, related to the natural curvature of the cornea and the focusing of the imaging beam. In this thesis, we try to compensate focusing problem using glass lens characteristic and stromal segmentation.

Using Glass Lens

A clear glass lens (Figure 5.13(a)) is used to compensate the focus problem explained in Chapter 4. We expect to see the same peaks at two sides of row intensity averaging of glass lens since the beam is focused on the back side of contact lens; two different peaks exist (Figure 5.13(b)). This difference peaks is used to correct the focal point of the corneal image by applying the inverse of difference (red dash line) to row averaged intensity of the flattened cornea. Figure 5.11 and Figure 5.14 show the row intensity averaging (I_r) before and after focal compensation respectively for patient 1.

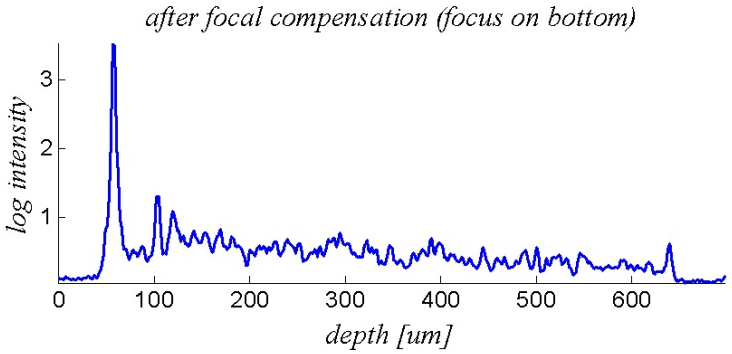

Figure 5.14: Row intensity averaging results of patient 1, after applying focal compensation to SNR corrected results in Figure 5.11 after applying glass lens focal compensation.

Using Stromal Segmentation

To account and compensate the image contrast variation [37] resulting from the corneal natural curvature and focusing effects, the stroma with thickness d in the flattened corneal image (Figure 5.15(b)) has been segmented to a predefine number of segments in the thickness of s_l. Then a Gaussian curve is fitted (which will be explained in Section 5.5) to each segment to be used in the segment intensity equalization to be applied to the middle third part of the same segment. Figure 5.15(c) shows the flattened corneal image after applying the inverse function to the stroma region. If the corrected stroma region (Figure 5.15(d)) is compared with the flattened cornea before correction, we observe less fluctuation than before since the contrast variation which is related to curvature and focusing effect has been compensated.

$$IS_k(i) = \sum_{(k-1)+\frac{sl}{3}}^{(k-1)+\frac{2s_l}{3}} I(i,j), \quad s.t. \quad s_l = \frac{d}{s_n} \tag{5.5}$$

where d is the stromal thickness and s_n and s_l are the number of segments and thickness of segments, respectively; $I(i,j)$ is the intensity value of each pixel in the corneal image and IS_k is the k^{th} column averaging intensity over middle third of k^{th} segment. The results in Figure 5.15 are based on 21 segments ($s_n = 21$). After stromal segmentation and column averaging intensity, we need to find the best Gaussian fit to the column averaging intensity to compensate the curvature and focus effect.

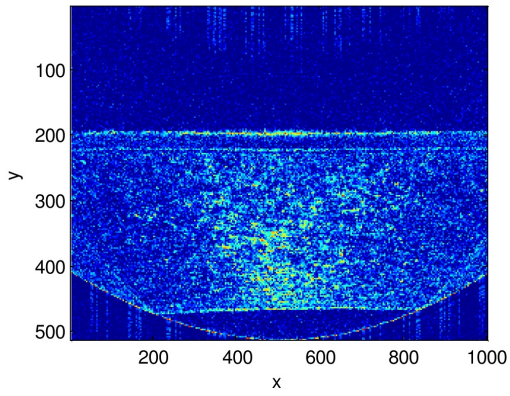

(a) Flattened corneal image

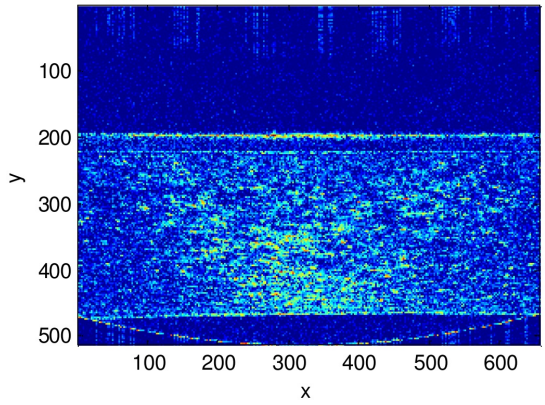

(b) Selected part of flattened corneal image with complete stromal region

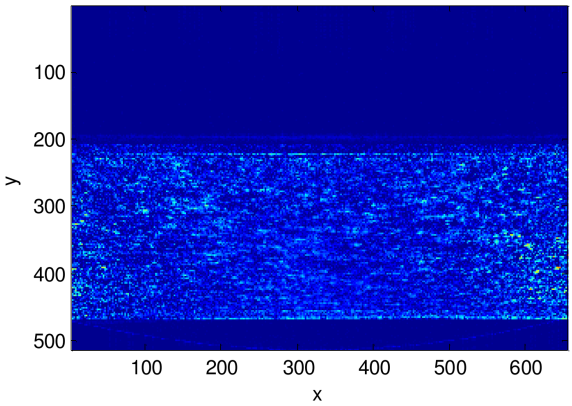

(c) Flattened corneal image after applying reverse of Gaussian fit to each stromal segment

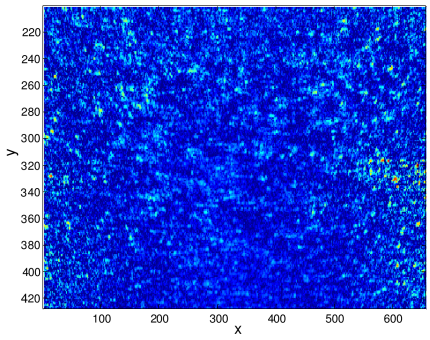

(d) Stromal region after focus and curve correction

Figure 5.15: To find a correct attenuation value, we need to remove the focus and curvature effects from the corneal image

5.5 Fitting

Empirically, the column averaging intensity shown in Figure 5.3(b) is Gaussian, so to correct for the spatial variations and the brightness increase caused by focusing, we wish to find the best Gaussian fit to the column averaging intensity of 50 rows on top and bottom parts of the stroma in the database shown in Figure 5.5. The Gaussian fitting is estimated by a maximum likelihood iteration, a coordinate descent on the three parameters of center (c), illumination peak (μ), and spatial standard deviation (σ). This joint optimization is driven by minimizing the mean square error between the Gaussian fit and the observed intensity values (Figure 5.16) calculated by the following equation

$$MSE(T) = \sum_{i=1}^{n} (I_c(i) - T)^2, \tag{5.6}$$

where I_c is the column averaged intensity, T is the target value of fitness case and n is the

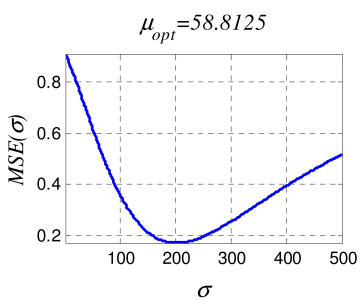

(a) Finding optimal σ by using initial center and μ

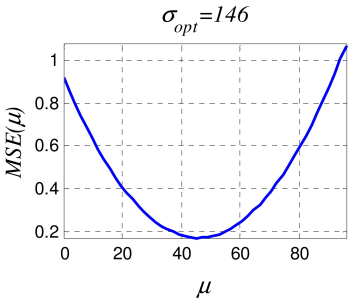

(b) Finding optimal μ by using optimal σ and initial center

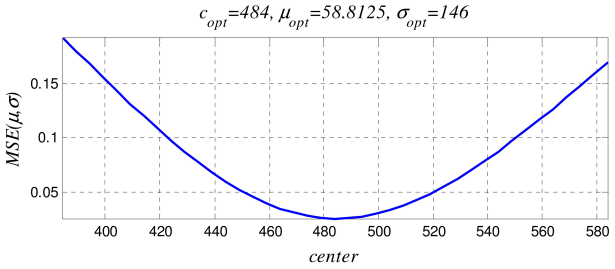

(c) Finding optimal center by using optimal σ and μ

Figure 5.16: Statistical Analysis – Finding optimum values of μ, σ and *center* to find the best Gaussian fit to Figure 5.3(b).

size of I_c. Figures 5.17 and 5.18 show two examples of the optimized Gaussian fits (red) given sample points (blue). Figures 5.19 and 5.20 show an overview and the block diagram of the proposed method, respectively.

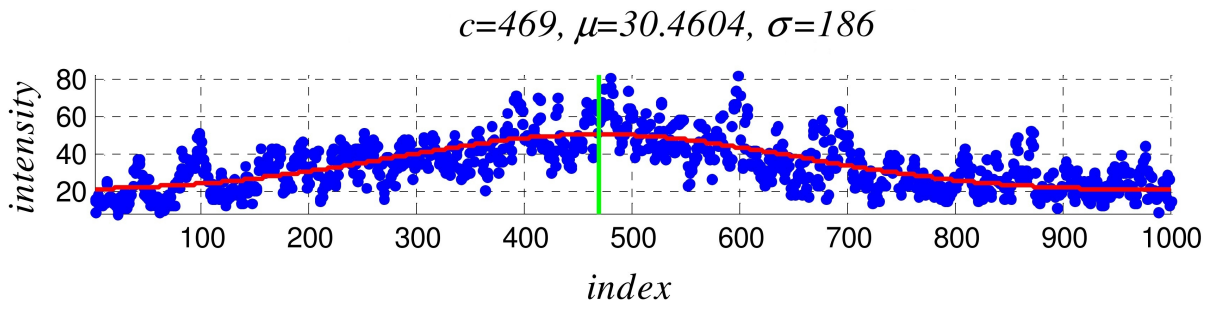

(a) Best Gaussian fit to the intensity distribution in the top part of stroma

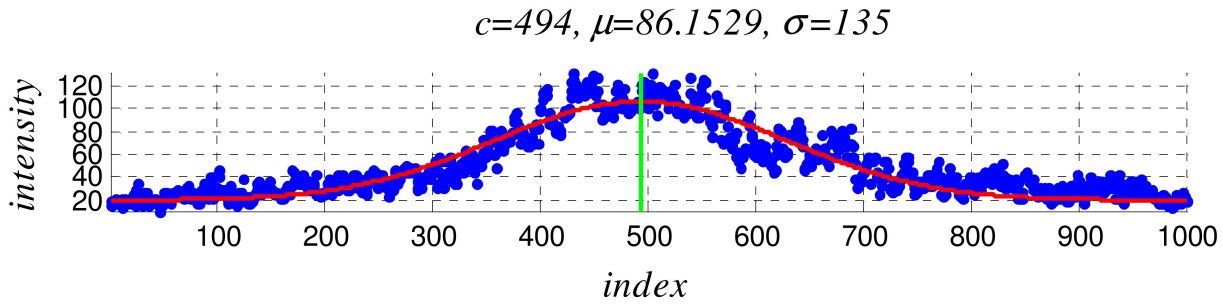

(b) Best Gaussian fit to the intensity distribution in the bottom part of stroma

Figure 5.17: The blue points show the average over each column of the straightened image, and the red curves show the best Gaussian fit, which is found from Figure 5.16, for each part (top and bottom) of the stroma.

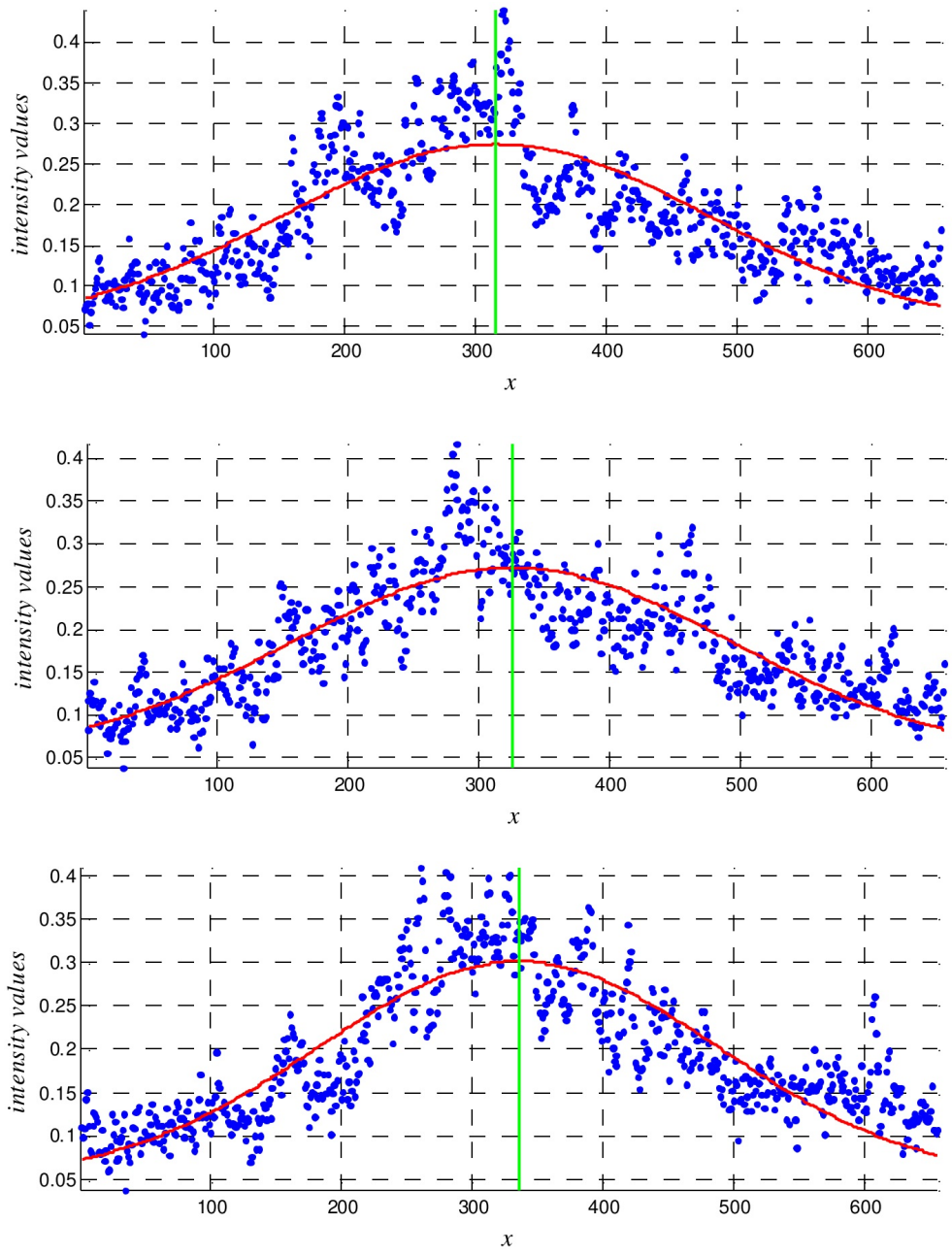

Figure 5.18: The blue points show the column intensity averaging of three consecutive segments of the stromal region in Figure 5.15, and the red curves show the best Gaussian fit, which acquired from Figure 5.16, for each segment of the stroma.

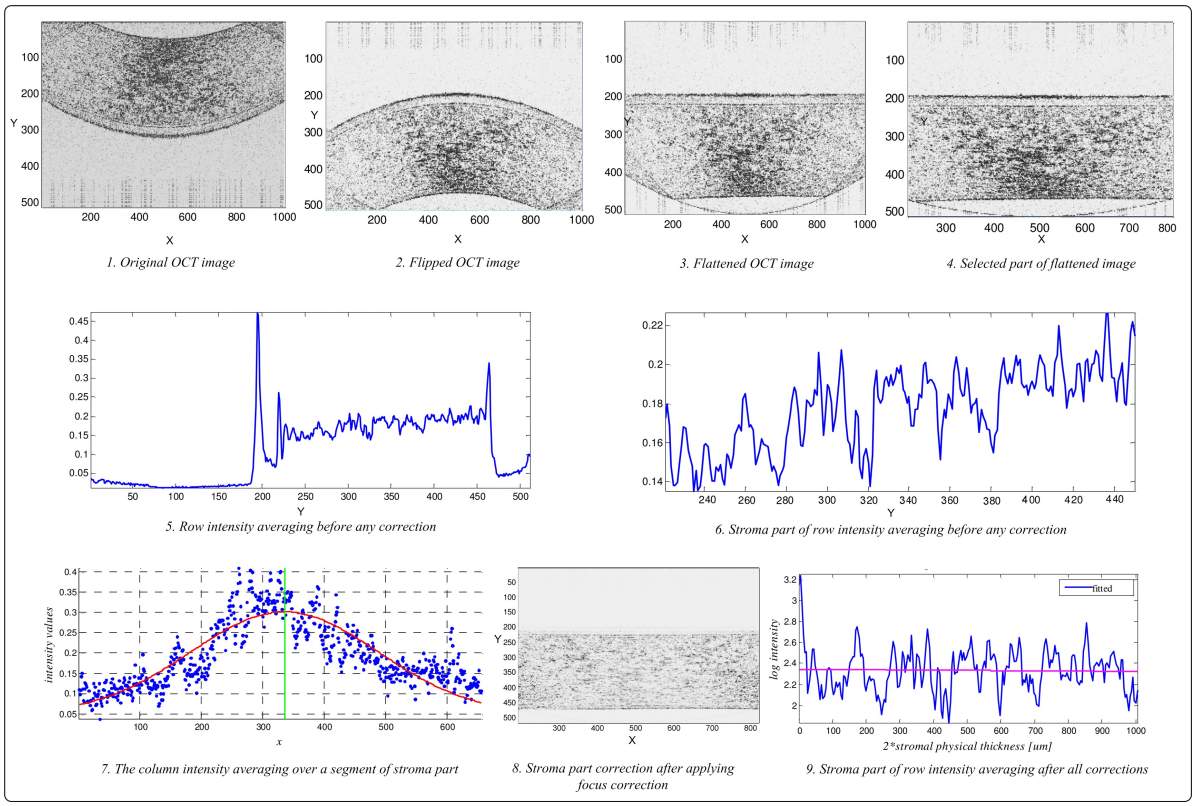

Figure 5.19: Snapshot of the proposed method for patient 3.

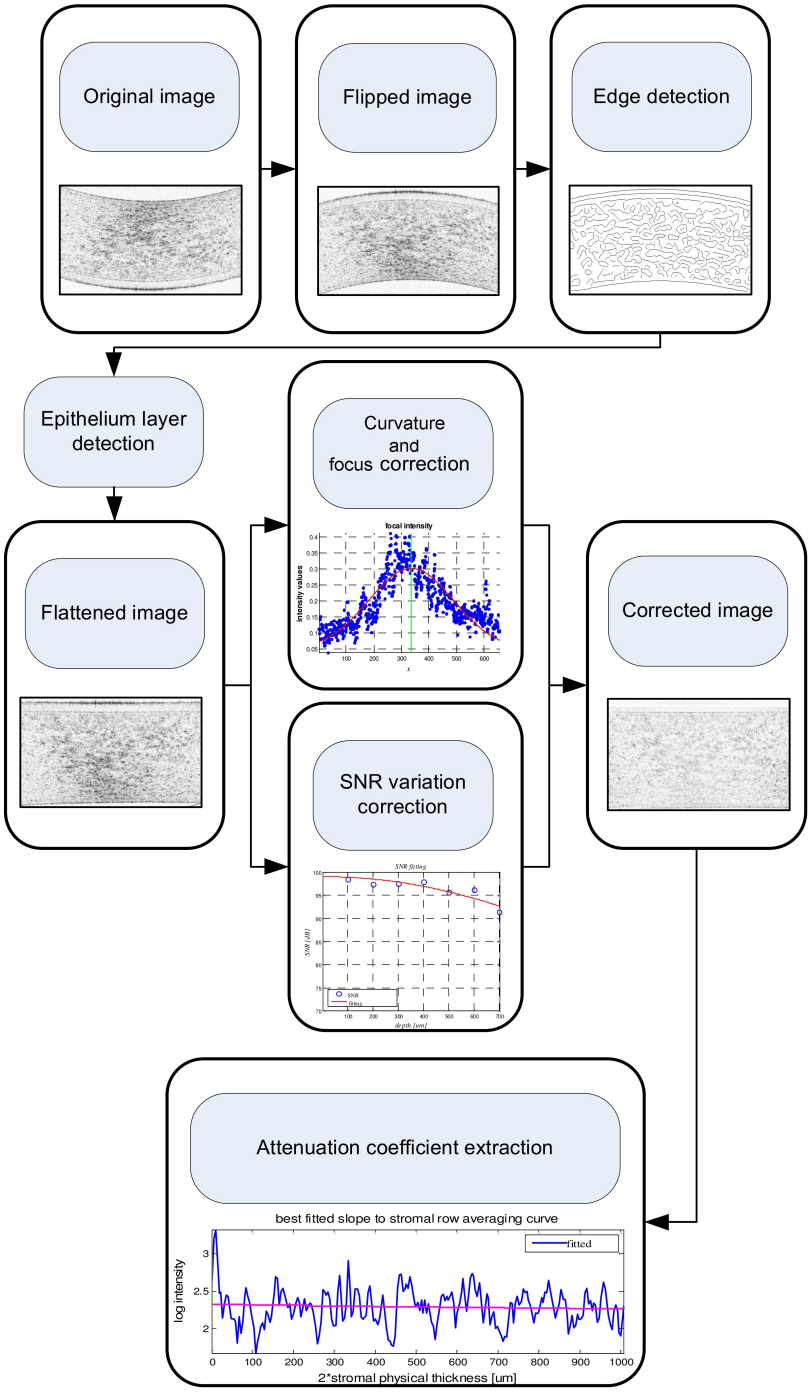

Figure 5.20: Block diagram – An enhanced image is acquired from OCT corneal image by processing the original image and applying mentioned correction algorithms on it.

Chapter 6

Results and Discussion

6.1 Statistical Analysis

As we mentioned in Chapter 4, a database of the corneal OCT images was used and compared attenuation coefficients in individuals. This section describes the proposed statistical inference scheme on the behavior of stromal attenuation and thickness over time.

Due to variations between individuals, over time, and instrument settings, significant variations exist in the received intensity. To investigate the attenuation coefficient variation over time after extracting the stromal intensity in Section 5.4, and finding the best Gaussian fit to the intensity in Section 5.5, a statistical analysis is needed.

6.1.1 Attenuation Coefficient Over Time

Figure 6.1 shows the attenuation coefficient results for three of the eight individuals, where the attenuation coefficient measures the slope of visual brightness which is correlated to hypoxia induced changes of the stroma. The horizontal axis indexes time, starting prior to insertion, immediately after the removal of the soft contact lens, and subsequently every 15 minutes for two hours. The vertical axis measures the attenuation coefficient, essentially the slope of the log-intensity image, in units of log-intensity per pixel. We expect to have positive attenuation coefficient (μ), but negative values have been depicted in Figure 6.1 which are compensated by applying SNR and focus correction, presented in Section 5.4.1 and 5.4.2, respectively. All of these results have almost the same trend. After wearing a contact lens (WL) the attenuation value is increased and after around two hours it comes

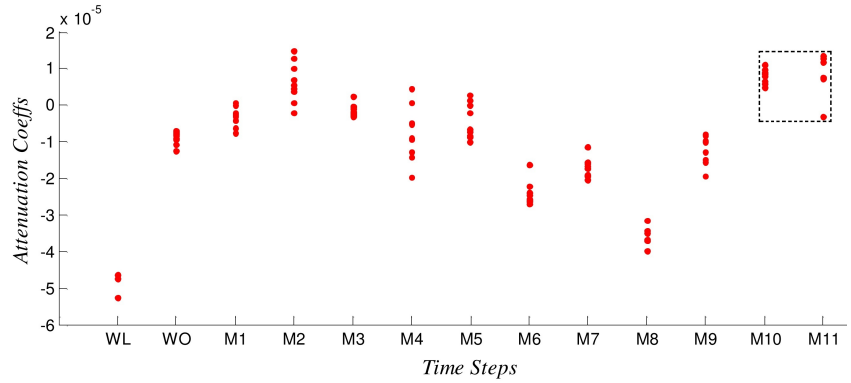

(a) Attenuation coefficients – Patient 1

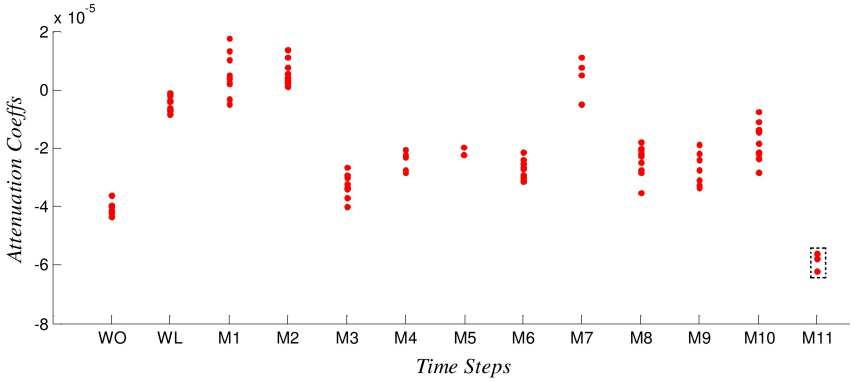

(b) Attenuation coefficients – Patient 2

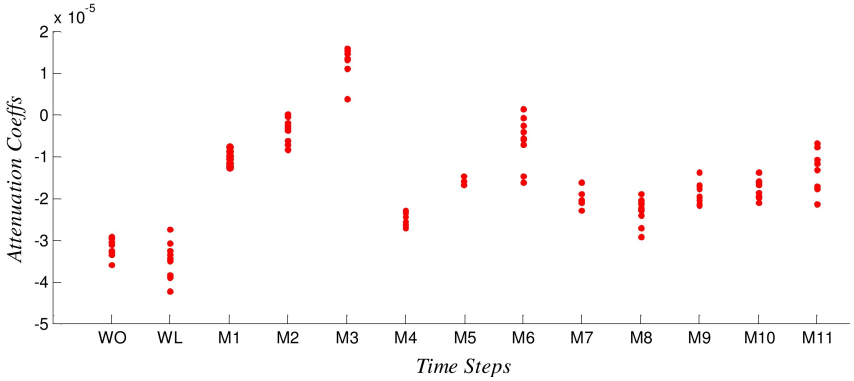

(c) Attenuation coefficients – Patient 3

Figure 6.1: Attenuation coefficient variation over time steps are increased after soft contact lens wear, with a recovery to baseline after roughly two hours, except two dashed marked last time steps in patient 1 (a) and last dashed marked step in patient 2 (b) due to unreliable OCT imaging.

back to the attenuation value before using contact lens (WL). We observe an unexpected behavior in M10 and M11 for patient 1 and also in M11 for patient 2. By looking at the OCT images in these particular time steps, some are blurred and some others are corrupted with eyelash artifacts, resulting in unreliable data. Therefore, we have removed these results from the evaluation. We want to compare the attenuation variation over time with statistical values variation of corneal images over time.

6.1.2 Mean and Standard Deviation Variations Over Time

From the maximum-likelihood Gaussian fit explained in Section 5.5, mean μ and standard-deviation σ of each corneal image are extracted from column intensity averaging results. Figure 5.17 shows the column intensity averaging of 50 rows on the top and bottom of the stroma – calculated by equation 5.2 – which belongs to patient 1 in time step WO. We want to find the correlation between the extracted attenuation coefficient and mean and standard deviation (σ) of each corneal image. Therefore, the mean and σ are extracted from the top and bottom of stromal region in column intensity averaging result. The top-bottom mean difference over different time steps is shown in Figure 6.2 which clearly correlates very closely with the attenuation plot of Figure 6.1(a). In both cases an unexpected behaviour is observed in the two end time steps (M10, M11) for patient 1 and in last time step (M11) for patient 2, almost certainly due to failures during image acquisition, which has been explained in Section 6.1.1.

Because a larger standard-deviation is associated with a greater spread in intensity, and therefore a reduced level of intensity, we anticipate a correction of $\mu \times \sigma$, if the signal is spread in one dimension, or $\mu \times \sigma^2$, if the spread is in fact in two dimensions, even if the measured corneal cross-section slices are along one dimension only. These corrected differences are shown in Figures 6.3 and 6.4, respectively. By this correction the variable, unexpected behavior is somewhat reduced. We observe, by using $\mu \times \sigma^2$ difference, the distance between two end unreliable time steps for patient 1 and last time step for patient 2 in Figure 6.1 are reduced by using $\mu \times \sigma^2$, even though the OCT images in these steps were noisy and inaccurate. Figure 6.4 shows that all individuals have quantitatively similar behavior, after wearing SCL (WL) the attenuation value is increased and after two hours it converges to a value. By these statistics we try to compensate the behaviour of attenuation coefficients.

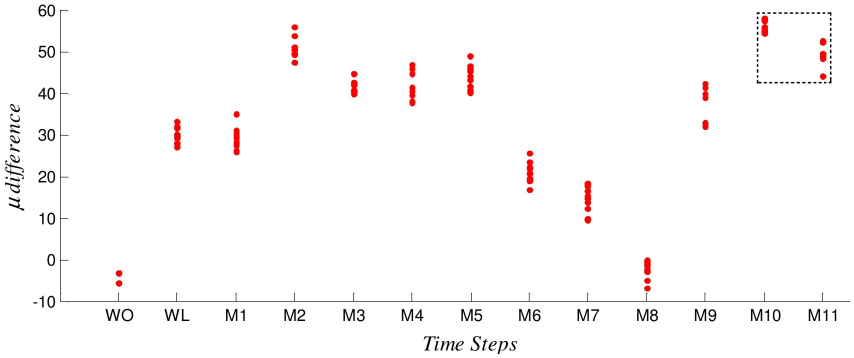

(a) μ difference of Patient 1

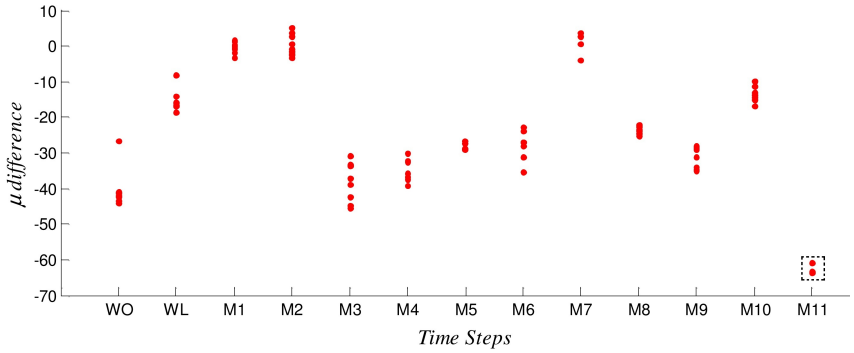

(b) μ difference of Patient 2

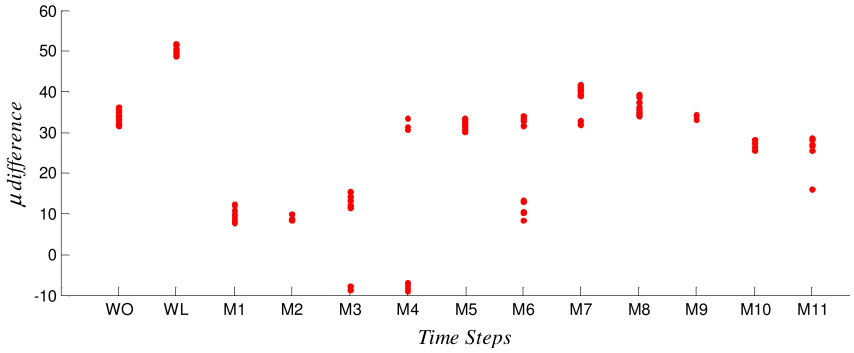

(c) μ difference of Patient 3

Figure 6.2: Difference between mean in the top and bottom segment of the stroma for three different individuals. The mean difference variation has the same behaviour as the attenuation coefficient in Figure 6.1.

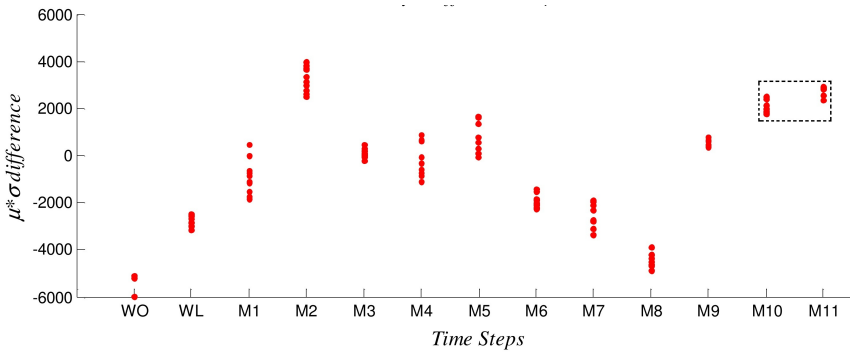

(a) $\mu \times \sigma$ difference of Patient 1

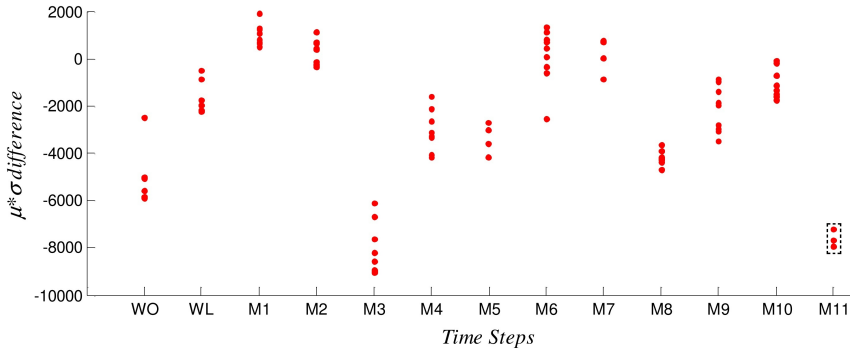

(b) $\mu \times \sigma$ difference of Patient 2

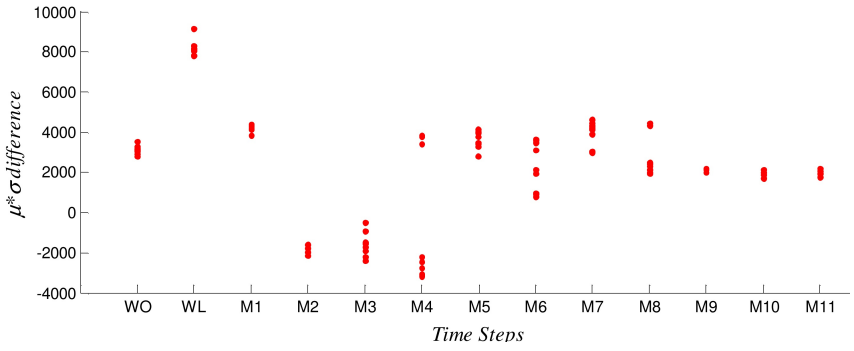

(c) $\mu \times \sigma$ difference of Patient 3

Figure 6.3: Difference between $\mu \times \sigma$ in top and bottom part of intensity for three individuals. This difference has attracted our attention since its behaviour is almost the same as the attenuation coefficient in Figure 6.1.

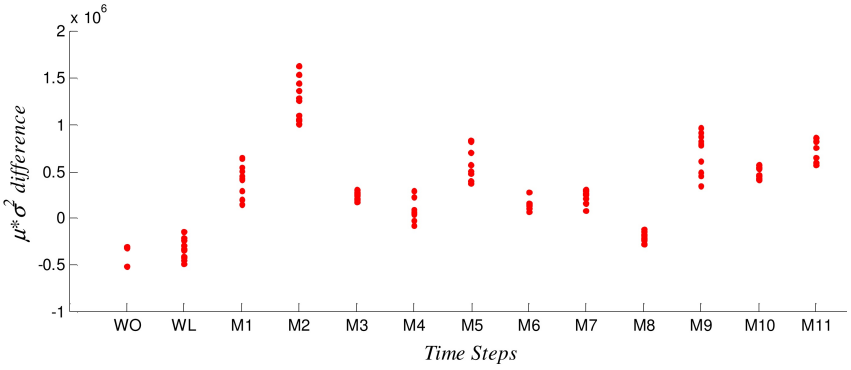

(a) $\mu \times \sigma^2$ difference of Patient 1

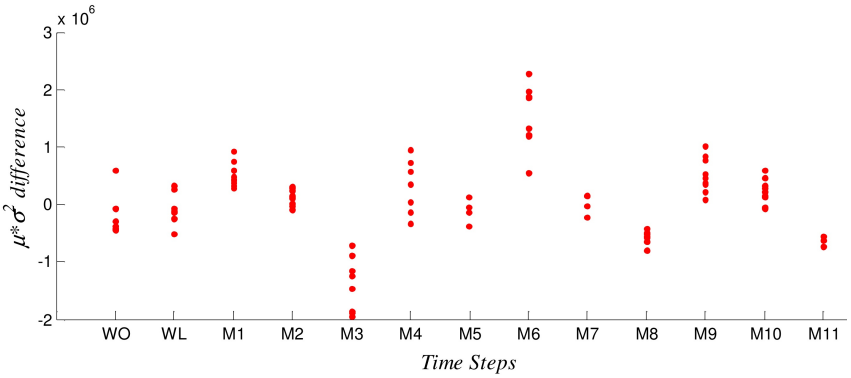

(b) $\mu \times \sigma^2$ difference of Patient 2

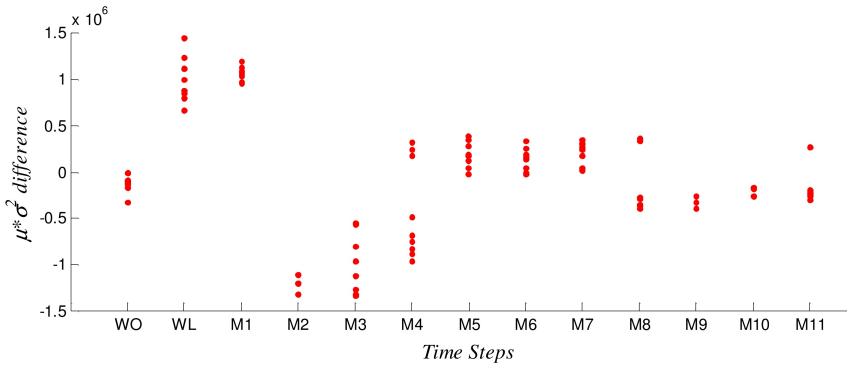

(c) $\mu \times \sigma^2$ difference of Patient 3

Figure 6.4: Statistical analysis – difference between $\mu \times \sigma^2$ in top and bottom part of three individuals. This difference has attracted our attention since the unexpected behaviour of three steps which have been marked in Figure 6.1and 6.3 are reduced.

6.1.3 Thickness Variations Over Time

For normal vision, it is imperative that the cornea maintains its high degree of transparency and physical characteristics, so the precise measurement of the thickness of the cornea is essential for the corneal swelling analysis. Since the cornea obtains oxygen directly from the air, and contact lenses lie between the cornea and the outside air, the corneal response to a contact lens is of considerable interest. Figure 4.3 on page 25 shown that the corneal thickness is changed before (WO) and immediately after removing the worn contact lens (WL) for three hours.

The variation in corneal thickness is very important since stromal thickness has influence on attenuation coefficients. Therefore, in this section, we analyze the stromal thickness behaviour over time steps for each individual. Figure 6.5 shows the stromal thickness variation of multiple individuals over 13 time steps. For all individuals, first the stromal thickness is gradually increased and after a while it comes back to the normal value (around WO). Time steps M10 and M11 have an unexpected behaviour in Figure 6.5(a) which is due to unsuccessful OCT imaging. If we ignore last two time steps in patient 1, the stromal thickness of all of the individuals have the same reaction to the contact lens.

The final results have a meaningful behavior, since separate analysis by optometric colleagues showed significant changes in the stroma's thickness [7, 17], observed immediately after the removal of the SCL, where the stromal thickness returned to baseline over a period of about two hours.

6.1.4 Standard Deviation Variation in Stromal Segments

To compensate focusing effect, the stromal region of the flattened corneal image is segmented to a predefined number of segments ($s_n = 21$). This value obtained by applying the different segment numbers on the image and finding the value which acquired best results. Column intensity averaging is calculated for each segment and the best Gaussian distribution is fitted to it as we mentioned in Section 5.5. In this section the standard deviation (σ) of these distributions are compared to investigate the intensity varition of each stromal segment in different time steps. In Figure 6.6, the stromal segments which are closer to the top of cornea (next to the epithelium), have the larger σ and the segments which are located at the bottom of the corneal image (next to the endothelium) have smaller values. This comparison shows the effect of focal illumination issue on standard deviation in each stromal segment. In Section 6.1.2, we observed the attenuation coefficients and statistical values are correlated, therefore it is important to know how σ varies from

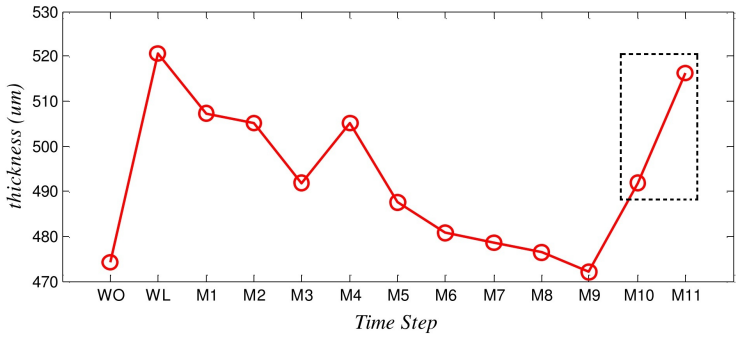

(a) Extracted stromal thickness for Patient 1

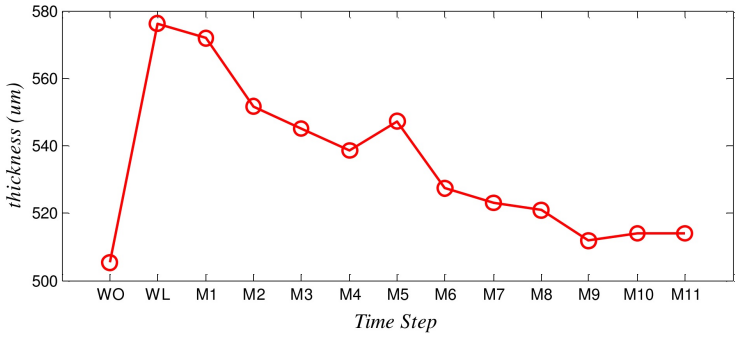

(b) Extracted stromal thickness for Patient 2

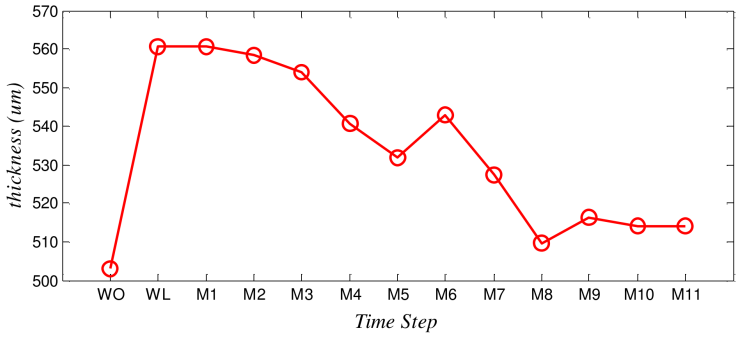

(c) Extracted stromal thickness for Patient 3

Figure 6.5: Stromal thickness variation over time – the stromal thickness is gradually increased and after a while it comes back to baseline, except for two last time steps for patient 1 due to invalid OCT image.

the top to the bottom of the corneal image. The top part of the corneal image has a larger σ value than the bottom part, also the maximum standard deviations occurs immediately after lens removal. The middle part of cornea has smoother variation in intensity and due to this smooth variation contains no useful information, therefore in Section 6.1.2 we only choose small segments of the top and bottom of cornea to analyze.

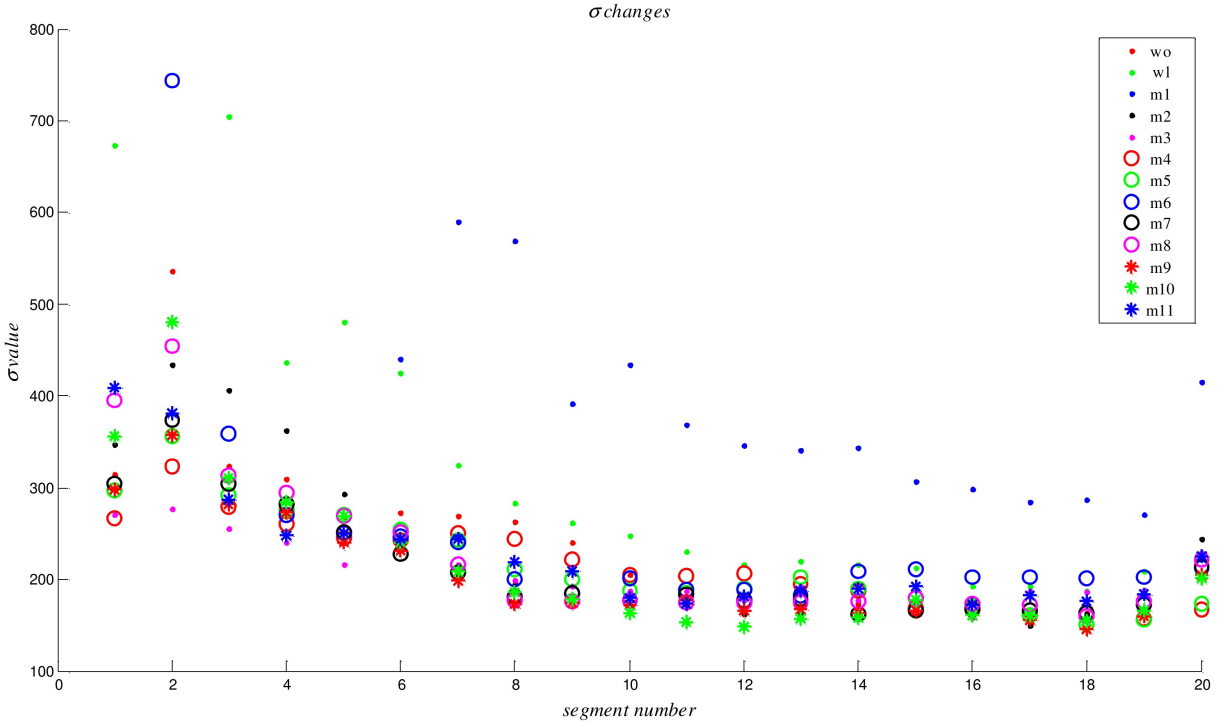

Figure 6.6: Statistical Analysis – σ varition of stromal segments in different time steps; the horizontal axis corresponds to the segment number in stroma region and the vertical axis shows the standard deviation value in each segment over different time steps. The maximum *sigma* difference is between top and bottom segments and the middle part of stroma has smoother variation in the intensity. It justifies our top and bottom segment selection in Figures 6.4 and 6.3

6.2 Hypoxia Results

About 10% stromal swelling was observed immediately after the removal of the SCL, while the stromal thickness returned to baseline in around two hours. Similarly, the stromal optical attenuation coefficient decreased over time with SCL wear and recovered to baseline in two hours after the lens removal. Figure 6.7 shows the variability of the attenuation coefficient of a subject over time with SCL wear and recovered to baseline in around two hours after the lens removal. Figure 6.8 compares the attenuation coefficients of three subjects over time. Figure 6.9 shows the average attenuation coefficient over three different subject as a function of time.

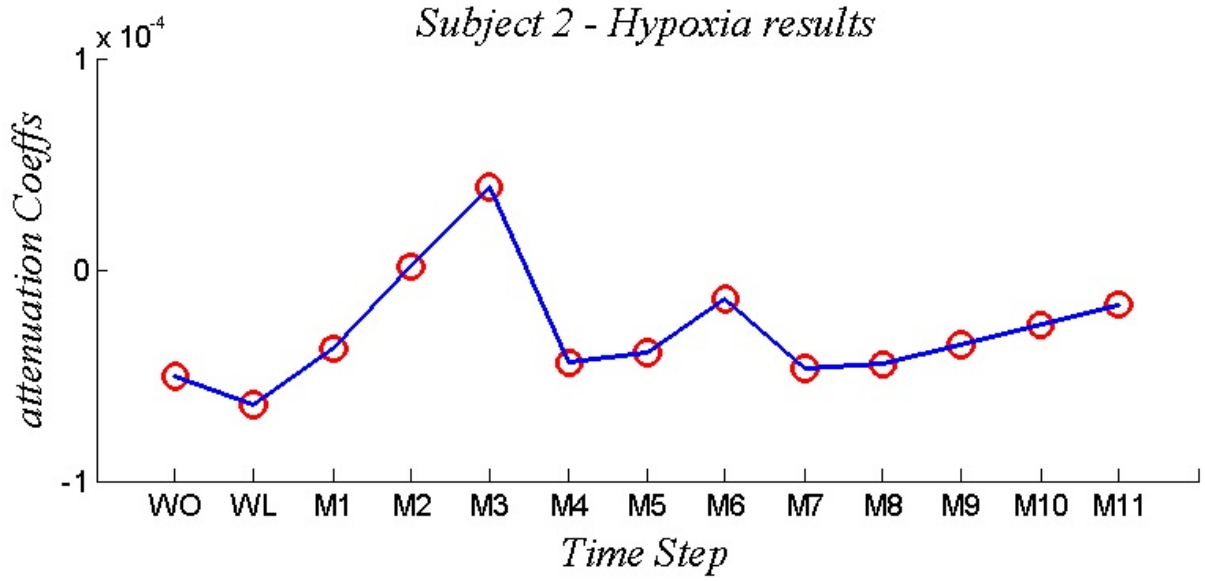

Figure 6.7: Hypoxia results of subject 2.

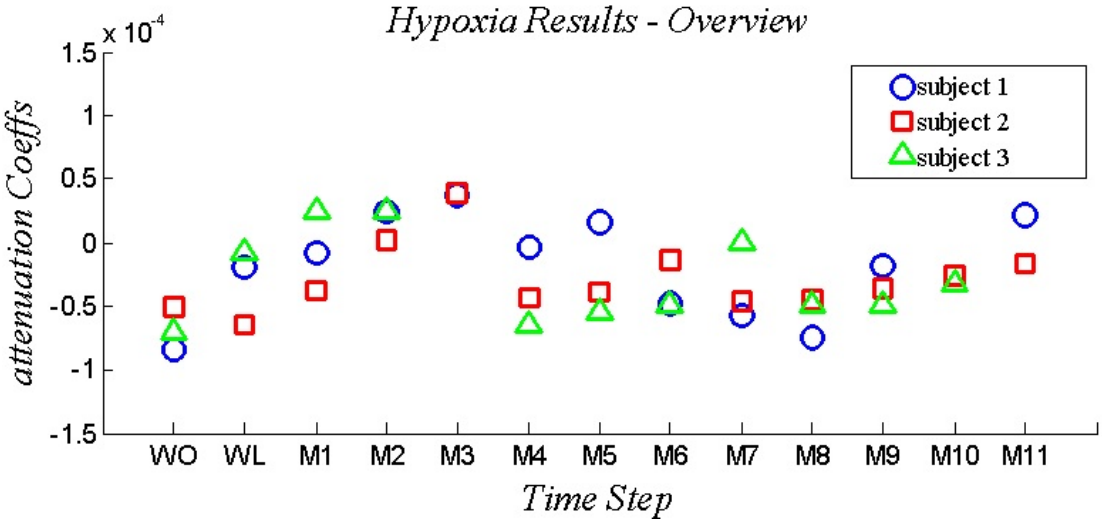

Figure 6.8: Hypoxia results of three subjects.

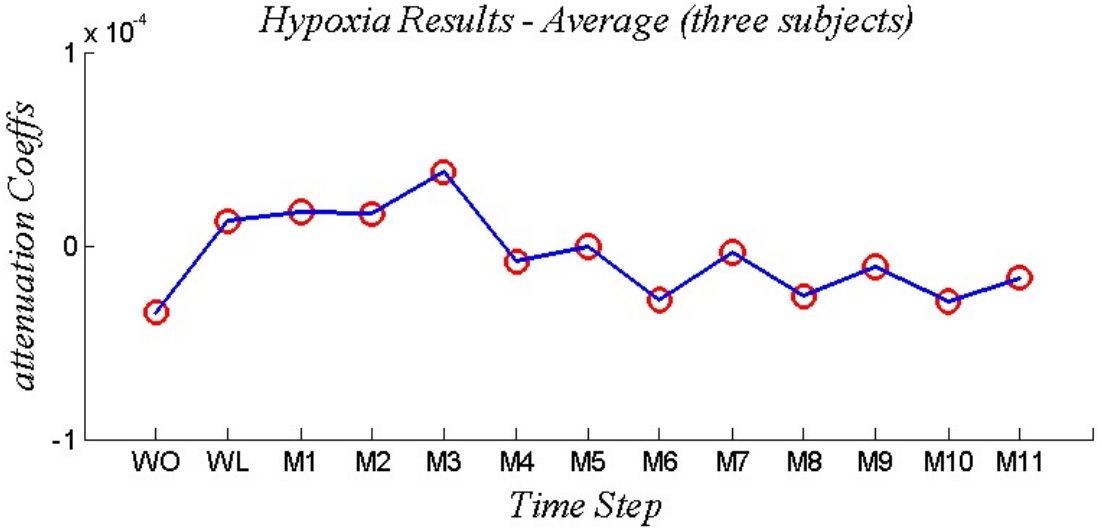

Figure 6.9: The average of Hypoxia results for three subjects which are shown in Figure 6.8.

Chapter 7

Conclusion and Future Work

In this thesis, we developed algorithms for segmenting the stroma, flattening of the cornea, compensation of the effect of the corneal curvature of the image SNR and contrast, as well as extracting the optical attenuation properties of the cornea from the OCT tomograms. We were given the hypoxia data to be able to test how our algorithms perform under different conditions and can they provide statistically significant measure of the attenuation changes cased by the hypoxia. We used a database of OCT images of the cornea for eight individuals by placing a soft contact lens (SCL) over the cornea and after removing the lens [17]. Due to variations between individuals, over time, and instrument settings, significant variations exist in the intensity pattern of the optical beam. A statistical analysis on the stromal intensity, fitting a distribution to the observed spatial variations, led to find out the attenuation coefficient variation over time.

Wearing a contact lens affects the corneal thickness and optical clarity. An automatic morphological segmentation is used to extract the actual thickness of stroma since corneal thickness has influence on attenuation coefficient. The attenuation coefficient (μ) is calculated by using Beer-Lambert's Law and related to incident intensity and transmitted light.

The depth-based SNR variation is one of the OCT device features that affects imaging and intensity values of cornea. We designed and applied the SNR correction scheme to corneal intensity. We also enhanced the corneal image and compensated focal effect to have a uniform distribution of compensated intensity in accurate extraction of μ. Since the SNR measurement was measured only one time, we were not make sure that the setting and measurement were same over the whole process, so this phase of correction was left out. We will have better results if we acquire another SNR measurement and apply the

SNR correction on the corneal images.

Another factor which affects the extracted attenuation coefficient is the spatial variation of contrast in the corneal image, related to the focusing of the imaging beam. The focusing problem was compensated by using glass lens and using stromal segmentation. The difference between two peaks at two sides of the glass lens were used to correct the focal point of the corneal image. Then the flattened cornea was segmented to a predefine number of segments and the column averaging intensity of each segment has been calculated and the Gaussian fit curve to it was used to find an inverse function applied to the middle third part of that particular segment. After all of these corrections, the attenuation coefficient was computed.

The proposed method also investigates features of the stromal region including probability distributions and their probable correlation in order to obtain a model for the attenuation coefficient variation among individuals.

A state-of-the-art, high speed, UHROCT system was used to acquire in-vivo images of the human cornea. For the first time we compensate the affect of curvature and focal plane of the optical beam with respect to the front or back surface of the cornea and get a clear corneal OCT image which can analyze its optical properties to investigate diseases with confidence.

Future work will attempt to have more accurate OCT imaging, since in this thesis some OCT images were corrupted because the subject has blinked during the imaging or due to wrong instrument setting. Also we will try to measure the exact SNR variation to compensate the focus problem precisely.

References

[1] G .B. Aboutanos, J. Nikanne, N. Watkins, and B. M. Dawant. Model creation and deformation for the automatic segmentation of the brain in MR images. *IEEE Trans. Biomed. Eng.*, 46(11):1346–1356, 1999. 11, 12, 23

[2] M. U. Akram, S. Nasir, A. Tariq, I. Zafar, and W. S. Khan. Improved fingerprint image segmentation using new modified gradient based technique. In *Canadian Conference on Electrical and Computer Engineering*, pages 1967–1972, 2008. 11

[3] G. Anthonys and N. Wickramarachchi. An image recognition system for crop disease identification of paddy fields in Sri Lanka. In *International Conference on Industrial and Information Systems*, pages 403–407, 2009. 11

[4] G. J. F. Banon, J. Barrera, and U. M. Braga-Neto. Mathematical morphology and its applicationsto signal and image processing. In *Proceedings of the 8th international symposium on mathematical morphology (ISSMM'07)*, 2007. 17, 18

[5] I. A. Barrera, C. G. Estrada, S. D. Zagal, and M. N. Perez. Segmentation of medical images by region growing. In *IEEE International Conference on Information Reuse and Integration*, pages 441–444, 2008. 13

[6] O. R. P. Bellon, A. I. Direne, and L. Silva. Edge detection to guide range image segmentation by clustering techniques. In *International Conference on Image Processing (ICIP2009)*, volume 2, pages 725–729, 1999. 12

[7] K. Bizheva, C. Hyun, J. Eichel, S. Hariri, A. Mishra, D. Clausi, P. Fieguth, T. Simpson, and N. Hutchings. Evaluation of hypoxic swelling of human cornea with high speed ultrahigh resolution optical coherence tomography. In *Proceedings of the SPIE*, volume 7163, Jan. 2009. 2, 3, 5, 28, 55

[8] S. H. Chang, L.Gong, M. Li, X. Hu, and J. Yan. Small retinal vessel extraction using modified canny edge detection. In *International Conference on Audio, Language and Image Processing*, pages 1255–1259, 2008. 13

[9] K. V. Chellappan, E. Erden, and H. Urey. Tlaser-based displays: a review. *Applied Optics*, 49(25):F79–F98, 2010. 19

[10] Y. B. Chen, O. T.-C. Chen, H. T. Chang, and J. T. Chien. An automatic medical-assistance diagnosis system applicable on x-ray images. In *Proc. of IEEE MWCAS2001*, volume 2, pages 910–914, 2001. 12, 23

[11] Z. Y. Chen, B. R. Abidi, D. L. Page, and M. A. Abidi. Gray-level grouping (GLG): An automatic method for optimized image contrast enhancementpart i: The basic method. *IEEE Transaction on Image Processing*, 15(8):2290–2302, 2006. 14

[12] Z. Y. Chen, B. R. Abidi, D. L. Page, and M. A. Abidi. Gray-level grouping (GLG): An automatic method for optimized image contrast enhancementpart ii: The variations. *IEEE Transaction on Image Processing*, 15(8):2303–2314, 2006. 14

[13] J. Cheng, R. Xue, W. Lu, and R. Jia. Segmentation of medical images with canny operator and gvf snake model. In *7th World Congress on Intelligent Control and Automation*, pages 1777–1780, 2008. 13

[14] V. Christopoulos, L. Kagemann, G. Wollstein, H. Ishikawa, M. L. Gabriele, M. Wojtkowskiand V. Srinivasan, J. G. Fujimoto, J. S. Duker, D. K. Dhaliwal, and J. S. Schuman. In vivo corneal high-speed, ultra high-resolution optical coherence tomography. *Archive of Ophthalmology*, 125:1027–1035, 2007. 5

[15] W. Drexler. Ultrahigh-resolution optical coherence tomography. *Journal of Biomedical Optics*, 9(1):47–74, Jan/Feb 2004. 1, 3, 5, 19

[16] W. D. Dupont. *Statistical Modeling for Biomedical Researchers: A Simple Introduction to the Analysis of Complex Data*. Cambridge Cambridge University Press, Reading, New York, 2002. 7

[17] J. Eichel, A. Mishra, D. Clausi, P. Fieguth, and K. Bizheva. A novel algorithm for extraction of the layers of the cornea. In *Canadian Conference on Computer and Robotic Vision (CRV)*, pages 313–320, May 2009. 1, 2, 22, 27, 28, 55, 60

[18] P. Fieguth. *Statistical Image Processing and Multidimensional Modeling*. Springer, New York, 2010. 7

[19] W. Gao, L. Yang, X. Zhang, B. Zhou, and C. Ma. Based on soft-threshold wavelet de-noising combining with prewitt operator edge detection algorithm. In *International Conference on Education Technology and Computer*, volume 5, pages 155–162, 2010. 13

[20] D. Huang, E. A. Swanson, C. P. Lin, J. S. Schuman, W. G. Stinson, W. Chang, M. R. Hee, T. Flotte, K. Gregory, C. A. Puliafito, and J. G. Fujimoto. Optical coherence tomography. *Science*, 254(5035):1178–1181, Nov. 1991. 1, 3, 5

[21] N. Hutchings, T. Simpson, C. Hyun, A. Moayed, S. Hariri, L. Sorbara, and K. Bizheva. Swelling of the human cornea revealed by high-speed, ultrahigh-resolution optical coherence tomography. *IVOS*, 51(9):4579–4584, Sept. 2010. 1, 5, 6, 7, 27

[22] J. A. Jiang, C. L. Chuang, Y. L. Lu, and C. S. Fahn. Mathematical-morphology-based edge detectors for detection of thin edges in low-contrast regions. *, The institution of engineering and technology (IET)*, 1(3):269–277, 2007. 2, 17

[23] M. Kass, A. Witkin, and D. Terzopoulos. Snakes: Active contour models. *International Journal of Computer Vision*, 1(4):321–331, 1988. 12, 23

[24] M. Kerker. *The Scattering of Light*. Academic Press, New York, 1969. 8

[25] M. Kim and Y. S. Ho. Semi-automatic segmentation by a double labeling method. In *Proc. of IEEE Region 10 Conference TENCON99*, volume 1, pages 746–749, 1999. 2, 12, 28

[26] S. Koompairojn, A. Petkova, K. A. Hua, and P. Metarugcheep. Semi-automatic segmentation and volume determination of brain mass-like lesion. In *IEEE International Symposium on Computer-Based Medical Systems*, pages 35–40, 2008. 12

[27] F. LaRocca, S. J. Chiu, R. P. McNabb, A. N. Kuo, J.A. Izatt, and S. Farsiu. Robust automatic segmentation of corneal layer boundaries in sdoct images using graph theory and dynamic programming. *Biomed Opt Express*, 2(6):1524–1538, June 2011. 28

[28] M. T. Lee and S. S. Chen. Image copyright protection scheme using sobel technology and genetic algorithm. In *International Symposium on Computer Communication Control and Automation*, pages 201–204, 2010. 13

[29] P. Lu, A. Stumpf, N. Kerle, and N. Casagli. Object-oriented change detection for landslide rapid mapping. *IEEE Geoscience and Remote Sensing Letters*, 8(4):701–705, 2011. 11

[30] R. Lu, P. Marziliano, and C. H. Thng. Liver tumor volume estimation by semi-automatic segmentation method. In *27th Annual International Conference of the Engineering in Medicine and Biology Society*, pages 3296–3299, 2005. 12

[31] L. W. MacDonald. Use of colour for image segmentation in the graphic arts. In *IEE Colloquium Binary Image Processing - Techniques and Applications*, pages 9/1–9/4, 1991. 12

[32] U. Maulik. Medical image segmentation using genetic algorithms. *IEEE Transaction on Information Technology in Biomedicine*, 13(2):166–173, 2009. 11

[33] A. A. Michelshon. *Studies in Optics*. University of Chicago, Chicago, IL, 1927. 16

[34] E. N. Mortensen and J. Jia. Real-time semi-automatic segmentation using a bayesian network. In *IEEE Computer Vision and Pattern Recognition*, volume 1, pages 1007–1014, 2006. 2, 12, 28

[35] C. Munteanu and A. Rosa. Gray-scale image enhancement as an automatic process driven by evolution. *IEEE Trans. Syst., Man and Cyber.*, 34(2):1292–1298, Apr. 2004. 14

[36] L. Najman and H. Talbot. *Mathematical Morphology: from theory to applications*. ISTE-Wiley, Hoboken, NJ, 2010. 17, 18

[37] J. P. Oakley and B. L. Satherley. Improving image quality in poor visibility conditions using a physical model for contrast degradation. *IEEE Transaction on Image Processing*, 7(2):167–179, 1998. 42

[38] Z. Pan and J. Lu. A bayes-based region-growing algorithm for medical image segmentation. *Computing in Science and Engineering*, 9(4):32–38, 2007. 11

[39] K. A. Panetta, J. Wharton, and S. S. Agaian. Human visula system-based image enhancement and logarithmic contrast measure. *IEEE Trans. Syst., Man and Cyber.*, 38(1):174–188, Feb. 2008. 14

[40] T. Pavlidis and Y. T. Liow. Integrating region growing and edge detection. *IEEE Transaction on Pattern Analysis and Machine Intelligence*, 12(3):225–233, 1990. 12

[41] E. Peli. Contrast in complex images. *Journal of the Optical Society of America A (JOSAA)*, 7(10):2032–2040, 1990. 14, 16

[42] D. L. Pham, C. Xu, and J. L. Prince. A survey of current methods in medical image segmentation. *Annual Review of Biomedical Engineering*, 2:315–337, 2000. 11

[43] I. Pitas. *Digital Image Processing Schemes and Application*. John Wiley and Sons, Inc., New York, 2000. 11, 12

[44] J. Pu, D. S. Paik, X. Meng, J. Roos, and G. D. Rubin. Shape "break-and-repair" strategy and its application to automated medical image segmentation. *IEEE Transaction on Visualization and Computer Graphics*, 17(1):115–124, 2010. 11

[45] P. Puvanathasan and K. Bizheva. Speckle noise reduction algorithm for optical coherence tomography based on interval type ii fuzzy set. *Opt. Express*, 15(24):15747–15758, 2007. 19

[46] P. Puvanathasan and K. Bizheva. Interval type-ii fuzzy anistropic diffusion algorithm for speckle noise reduction in optical coherence tomography images. *Opt. Express*, 17(2):733–746, 2009. 19

[47] P. Puvanathasan, P. Forbes, Z. Ren, D. Malchow, S. Boyd, and K. Bizheva. High-speed, high-resolution fourier-domain optical coherence tomography system for retinal imaging in the 1060 nm wavelength region. *Opt lett*, 33(21):2479–2481, Nov. 2008. 5

[48] J. Rogowska and M. E. Brezinski. Evaluation of the adaptive speckle suppression lter for coronary optical coherence tomography imaging. *IEEE Trans. Med. Imaging*, 19:1261 –1266, 2000. 7

[49] E. Romero, O. Cuisenaire, P. Moulin, and B. Macq. A semi-automatic approach to measurement of pancreatic endocrine volume tissue density. In *Proceedings of the IEEE-EMBS Special Topic Conference on Molecular, Cellular and Tissue Engineering*, pages 184–185, 2002. 11

[50] J. C. Russ. *The image processing handbook*. CRC Press, Boca Raton, FL, sixth edition, 2010. 14

[51] J. M. Schemitt, S. H. Xiang, and K. M. Yung. Speckle in optical coherence tomography. *Journal of Biomedical Optics*, 4(1):95–105, 1999. 19

[52] M. P. Segundo, L. Silva, O. R. P. Bellon, and C. C. Queirolo. Automatic face segmentation and facial landmark detection in range images. *IEEE Transaction on Systems, Man, and Cybernetics*, 40(5):1319–1330, 2010. 11

[53] D. A. Skoog. *Fundamentals of Analytical Chemistry.* Saunders College Publishing, New York, 1997. 8

[54] P. Soille. *Morphological Image Analysis; Principles and Applications (2nd edition).* Springer, Heidelberg, Berlin, 2003. 17

[55] P. Sutthiwichaiporn, V. Areekul, and S. Jirachaweng. Iterative fingerprint enhancement with matched filtering and quality diffusion in spatial-frequency domain. In *International Conference on Pattern Recognition (ICPR)*, pages 1257–1260, 2010. 14

[56] W. G. Tam and A. Zardecki. Multiple scattering corrections to the Beer-Lambert law. 1: Open detector. *Applied Optics*, 21:2405–2412, 1982. 8

[57] H. Tasmaz and E. Ercelebi. Image enhancement via space-adaptive lifting scheme using spatial domain adaptive wiener filter. In *Proceedings of 6th International Symposium on Image and Signal Processing and Analysis*, pages 287–292, 2009. 14

[58] S. Teranishi, K. Kimura, K. Kawamoto, and T. Nishida. Protection of human corneal epithelial cells from hypoxia induced disruption of barrier function by keratinocyte growth factor. *Invest Ophtalmol Vis Sci*, 49(6):2432–2437, 2008. 27

[59] Y. Tian, Q. Wan, and F. Wu. Local histogram equalization based on the minimum brightness error. In *Fourth International Conference on Image and Graphics, 2007 (ICIG 2007)*, pages 58–61, 2007. 14, 34

[60] J. I. Trisnadi. Speckle contrast reduction in laser projection displays. *Proc. SPIE*, 4657(Projection Displays VIII):131–137, 2002. 19

[61] S. E. Umbaugh, R. H. Moss, and W. V. Stoecker. Automatic color segmentation of images with application to detection of variegated coloring in skin tumors. *IEEE Engineering in Medicine and Biology Magazine*, 8(4):43–50, 1989. 11

[62] S. Y. Wan and W. E. Higgins. Symmetric region growing. *IEEE Trans. Image Processing*, 12(9):1007–1015, 2003. 12

[63] J. Wang, T. L. Simpson, and D. Fonn. Objective measurements of corneal light-backscatter during corneal swelling, by optical coherence tomography. *Invest Ophthalmol Vis Sci.*, 45(10):3493–3498, 2004. 1, 3

[64] J. S. Weszka, R. N. Nagel, and A. Rosenfeld. A threshold selection technique. *IEEE Transaction Computer*, 23:1322–1326, 1974. 12

[65] R. R. Wilcox. *Fundamentals of Modern Statistical Methods: Substantially Improving Power and Accuracy*. Springer, New York, 2001. 7

[66] K. Wong, P. Heng, and T. Wong. Taccelerating 'intelligent scissors' using slimmed graphs. *Journal of Graphics Tools*, 5(2):1–13, 2000. 12

[67] C. Xu and J. Prince. Snakes, shapes and gradient vector flow. *IEEE Trans. on Image Processing*, 7(3):359–369, 1998. 12

[68] Y. Xu, J. Zhao, and Y. Jiao. Noisy image edge detection based on multi-scale and multi-structuring element order morphology transformation. In *CISP'08*, volume 3, pages 379–383, 2008. 2, 17

[69] H. Zhu, H. Y. Chan, and F. K. Lam. Image contrast enhancement by constrained local histogram equalization. *Computer Vision and Image Understanding*, 73(2):281–290, Feb. 1999. 14, 34

[70] S. W. Zucker. Region growing: childhood and adolescence. *Computer Graphics Image Processing*, 5:382–399, 1976. 12, 13

[71] K. Zuiderveld. *Contrast limited adaptive histogram equalization*, pages 474–485. Graphics Gem IV, Cambridge, MA, P. S. Heckbert edition, 1994. 16